博士学位論文

On a mathematical modeling and a computer-aided analysis for self-propelled systems
（自己駆動系に対する数理モデリングと計算機援用解析について）

安ヶ平　裕介

北海道大学大学院理学院
数学専攻

２０２２年６月

On a mathematical modeling and a computer-aided analysis for self-propelled systems

Yusuke YASUGAHIRA

June 2022

Contents

I On a numerical bifurcation analysis of a particle reaction-diffusion model for a motion of two self-propelled disks 3

1 Introduction 3

2 Mathematical Definitions of Disk Motions 6

3 Numerical Results 9
3.1 Newfound motions and their definitions 9
3.2 Bifurcation Diagram 12

4 Analysis of the Chaotic Motion 14

5 Conclusion 18

A Discretization 18

B Numerical methods 25
B.1 Time integration 25
B.2 Pseudoarclength Method 26
B.3 Calculation of Jacobian Matrix 28

II Catch and Release Chemotaxis 34

1 Introduction 34

2 Experimental Results 34

3 Discussion 36

4 Conclusion 43

A Miscellaneous Experimental Setup 45

Part I
On a numerical bifurcation analysis of a particle reaction-diffusion model for a motion of two self-propelled disks

1 Introduction

Since the work of T. Vicsek et al., many theoretical analyses using particle motion models have been performed to understand the collective motion of biological species [1]. For example, flocks of birds [2], schools of fish [3], and insect swarms [4] have been investigated. In addition, physicists have developed many mathematical models of collective motion assuming various interactions [6–11]. Recently, there is also an analysis of collective motion that considers non-local interactions [12]. Moreover, spontaneous motions of non-living systems have been reported, such as collective motions using liquid crystal molecules [13], micotubes [14, 15], asymmetric particles called Janus colloidal particles [17] on the micromere scale [18], millimeter rods [16], etc.

In particular, there is a macroscopic experimental system called a self-propelled system in which individual materials move by changing the state of the field. For example, camphor particles [19] and oil droplets [20, 21] move in translational motion by changing the surface tension of the water.

Many types of research have been performed to understand the mechanism of collective motions using such self-propelled systems, and collective motions on annular water channels using camphor boats and camphor disks [22, 23] and on the water surface of petri dishes [24–26] have been reported. In addition, a self-assembly motion of droplets has been reported by using the chemical reaction [27]. The mathematical model has also been proposed to understand the collective motion for such macroscopic self-propelled material. For example, there is a mathematical model for the collective motion of camphor boats in the annular water channel [28] and the collective oscillatory motion of camphor disks [29], and there is also a mathematical model for the self-assembly motion of droplets with the chemical reaction [30].

One of the mathematical models to describe the above motion of self-

propelled material is the particle reaction-diffusion model as follows [31]:

$$\begin{aligned} \rho\frac{d^2x_c^i}{dt^2} &= G(u(x_c^i(t),t)) - \mu\frac{dx_c^i}{dt}, \\ \frac{\partial u}{\partial t} &= d_u\frac{\partial^2 u}{\partial x^2} - ku + \sum_{i=1}^{N} F(x - x_c^i(t)), \end{aligned} \tag{1}$$

where $x_c^i(t)$ and $u(x,t)$ are the center of an i-th disk, which is the surfactant and a surface concentration of the surfactant, respectively. ρ, μ, d_u and k denote an area density of the disk, a friction coefficient, a diffusion coefficient of surfactant molecules on a water surface, and a combined rate of sublimation and dissolution of the surfactant, respectively. When $N = 1$, (1) represents the motion of a single self-propelled material, and when $N \geq 2$, it represents the collective motion of self-propelled material. The function $G(u)$ is a driving force to the self-propelled material, which is given by, for example,

$$G(u) = \frac{1}{2r}\left(\gamma(u(x_c(t)+r,t)) - \gamma(u(x_c(t)-r,t))\right),$$

or

$$G(u) = \left.\frac{d\gamma(u(x,t))}{dx}\right|_{x=x_c(t)}.$$

where the function $\gamma(u) > 0$ describe the surface tension on the water surface, for instance, which is the following strictly decreasing function of $u > 0$:

$$\gamma(u) = \frac{a^m}{a^m + u^m}(\gamma_0 - \gamma_1) + \gamma_1, \tag{2}$$

where $a > 0$, $m \in \mathbb{N}$, and γ_0, $\gamma_1 > 0$ represent the surface tension of pure water and that of the critical micelle concentration of the surfactant, respectively. The function $F(x)$ represents the supply of the surfactant molecules, and a simple example of it is the supply from solid surfactant, which is described by

$$F(x) = \begin{cases} k_u u_0, & |x| \leq r, \\ 0, & |x| > r, \end{cases} \quad \text{or} \quad F(x) = k_u u_0 \delta(x),$$

where k_u and u_0 are the supply rate and the density of the solid surfactant, respectively, and r is the radius of the solid surfactant. $\delta(x)$ is the Dirac delta function, corresponding to the point source. In order to theoretically understand the mechanism of self-propelled material motion, much computer-aided and formal analysis using mathematical models have been investigated [32–36]. Furthermore, as rigorous mathematical analysis of the mathematical model(1), the global existence of solutions in the whole space and the existence of unique traveling wave solutions [37], rotational motion

solutions for one-dimensional periodic boundary conditions in space have been shown for the piecewise constant function supply term [38]. In addition, the existence of weak solutions is shown for the delta function supply term [39]. To understand the collective motion of camphor disks in the annular water channel [40], in 2015 Nishi et al. analyzed the interaction of two camphor disks using the following dimensionless mathematical model without the inertia term, which assumes that camphor disks are very light [41]:

$$\begin{aligned} \mu \frac{dx_c^i}{dt} &= \frac{\gamma(u(\pi_L(x_c^i + r), t)) - \gamma(u(\pi_L(x_c^i - r), t))}{2r}, \\ \frac{\partial u}{\partial t} &= \frac{\partial^2 u}{\partial x^2} - u + \sum_{i=1}^{N} F(x - x_c^i), \end{aligned} \tag{3}$$

for $i = 1, \cdots, N$, and $x \in [-L/2, L/2)$, where $\mu > 0$ and $L > 2Nr > 0$, and the function $\gamma(u)$ and $F(x)$ are given by

$$\gamma(u) = \frac{a^2}{a^2 + u^2} + \frac{\gamma_1}{\gamma_0 - \gamma_1}, \tag{4}$$

$$F(x) = \begin{cases} 1, & |x|_L \le r, \\ 0, & |x|_L > r, \end{cases} \qquad |x|_L = \min_{n \in \mathbb{Z}} |x + nL|, \tag{5}$$

$$\pi_L(x) = \begin{cases} \pi_L(x - L), & x \ge L/2, \\ \pi_L(x + L), & x < -L/2, \\ x, & \text{otherwise}, \end{cases} \tag{6}$$

where a, γ_0, γ_1 are positive constants. π_L is a map from $\mathbb{R}$ to $[-L/2, L/2)$ that is equivalent to a canonical projection $\mathbb{R} \to \mathbb{R}/\mathbb{Z} \cong S^1$ to which the annular water channel is considered to be homeomorphic. When $N = 2$, from the computer-aided analysis of (3) under the periodic boundary condition and the additional experimental results, the model system(3) was shown to qualitatively reproduce well the motion of two camphor disks [41]. The results also suggest that the traffic jam motion and billiard-like motions reported in the experiments can be reproduced. They are reproduced qualitatively, as shown in Fig.1. In this study, the existence and stability of the motionless solution, the symmetric rotating solution (Fig.2(a)), and the asymmetric rotating solution (Fig.2(b)) have also been investigated by computer-aided analysis. In addition, characteristic numerical results such as an asymmetric oscillatory solution(Fig.3(a)), an oscillatory rotating solution(Fig.3(b)(c)) and an irregular motion solution(Fig.3(d)) have been shown, but the bifurcation mechanism by which these solutions emerge is not known.

In our study, we theoretically show the mechanism of the emergence of complex motions by analyzing the global bifurcation structure of (3) on the

annular water channel when $N = 2$ and $L = 10$, using the numerical bifurcation method. Furthermore, the bifurcation mechanism in which irregular motions appear is explained, and the chaotic nature of irregular motions is clarified by numerical calculation of the maximum Lyapunov exponent. This paper is organized as follows: the solution to be obtained by the numerical bifurcation is defined in Chapter 2. In Chapter 3, based on the definition of the solution, numerical solutions are obtained by the bifurcation method, and the linearization stability of the solutions is also shown numerically. In Chapter 4, we discuss the results of the bifurcation structure in Chapter 3 and focus on irregular motions to investigate the mechanism of their appearance. Finally, we summarize the entire study and discuss future work.

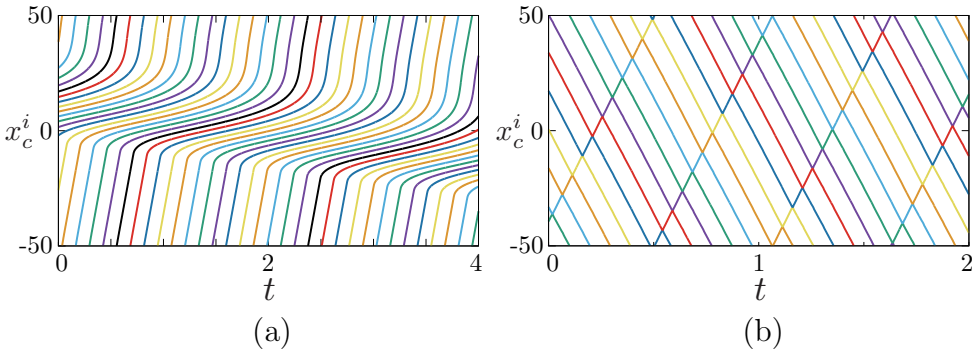

Figure 1: (a) The trajectory of the asymptotic solution $x_c^i (1 \leq i \leq 14)$ corresponding to an traffic jam like motion of camphor disks. (b) The trajectory of the asymptotic solution $x_c^i (1 \leq i \leq 7)$ corresponding to an billiard like motion of camphor disks. Both solutions are obtained by the numerical computation for (3) with $\mu = 0.0002$, $r = 0.5$, $L = 100$, $m = 2$ and $a = 0.05$.

2 Mathematical Definitions of Disk Motions

To analyze motions of disks on annular water channel, we introduce mathematical equations of which solutions correspond to actual motions. Firstly, we change the coordinate system of (3) from stationary to moving coordinate system $z = x - ct$ where c represents a system velocity, which allows us to treat rotating motions such as the ones shown in Fig.2 as stationary solutions. As the result of the transformation, we obtain the following

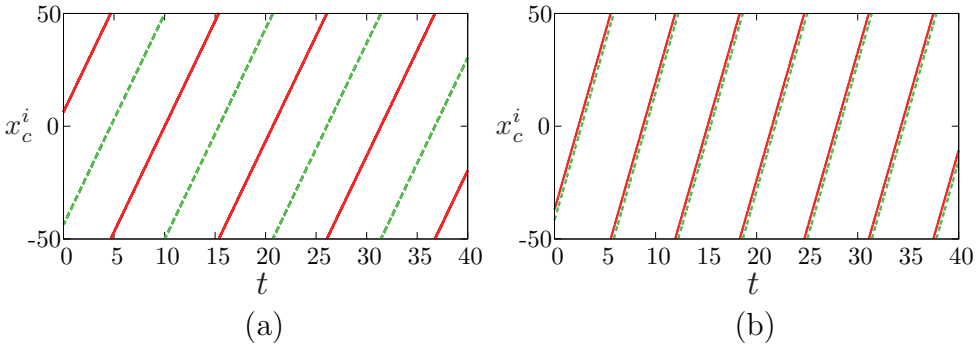

Figure 2: The trajectory of the asymptotic solution x_c^1 and x_c^2. The solid and dashed lines represent the trajectories of x_c^1 and x_c^2, respectively. (a) A symmetrically rotating solution of two disks ($\mu = 0.08$), (b) An asymmetrically rotating solution of two disks ($\mu = 0.01$). Both solutions are obtained by the numerical computation for (3) with $r = 0.5$, $L = 100$, $m = 2$ and $a = 0.05$.

equations:

$$\begin{aligned} \mu \frac{dz_c^i}{dt} &= \frac{\gamma(v(\pi_L(z_c^i + r), t)) - \gamma(v(\pi_L(z_c^i - r), t))}{2r} - \mu c, \\ \frac{\partial v}{\partial t} &= \frac{\partial^2 v}{\partial z^2} - c\frac{\partial v}{\partial z} - v + \sum_{i=1}^{N} F(z - z_c^i), \end{aligned} \tag{7}$$

where $v(z,t) = u(z + ct, t)$ and $z_c^i(t) = x_c^i(t) - ct (i = 1, ..., N)$. We define four types of motion as solutions of mathematical equations using (7). Note that we denote concentration profile, position of disks, system velocity, temporal period and the region $[-L/2, L/2)$ by v, z_c^i, c, T and I, respectively.

Definition 1 (Motionless solution)**.** *A tuple* $(v, z_c^1, ..., z_c^N, c) \in C^1(I; (0,\infty)) \times C^1(0,\infty)^N \times \mathbb{R}$ *is called a motionless solution if* $c = 0$ *and* $(v, z_c^1, ..., z_c^N)$ *is a stationary solution of* (7) *with system velocity* $c(= 0)$*.*

Definition 2 (Rotating solution)**.** *A tuple* $(v, z_c^1, ..., z_c^N, c) \in C^1(I; (0,\infty)) \times C^1(0,\infty)^N \times \mathbb{R}$ *is called a rotating solution if* $c \neq 0$ *and* $(v, z_c^1, ..., z_c^N)$ *is a stationary solution of* (7) *with system velocity* c*.*

Definition 3 (Oscillatory solution)**.** *A tuple* $(v, z_c^1, ..., z_c^N, c, T) \in C^1(I; (0,\infty)) \times C^1(0,\infty)^N \times \mathbb{R} \times \mathbb{R}$ *is called an oscillatory solution if* $c = 0$ *and* $(v, z_c^1, ..., z_c^N)$ *is a time-periodic solution of* (7) *with system velocity* $c(= 0)$ *and period* $T > 0$*.*

Definition 4 (Oscillatory rotating solution)**.** *A tuple* $(v, z_c^1, ..., z_c^N, c, T) \in C^1(I; (0,\infty)) \times C^1(0,\infty)^N \times \mathbb{R} \times \mathbb{R}$ *is called an oscillatory rotating solution if* $c \neq 0$ *and* $(v, z_c^1, ..., z_c^N)$ *is a time-periodic solution of* (7) *with system velocity* c *and period* $T > 0$*.*

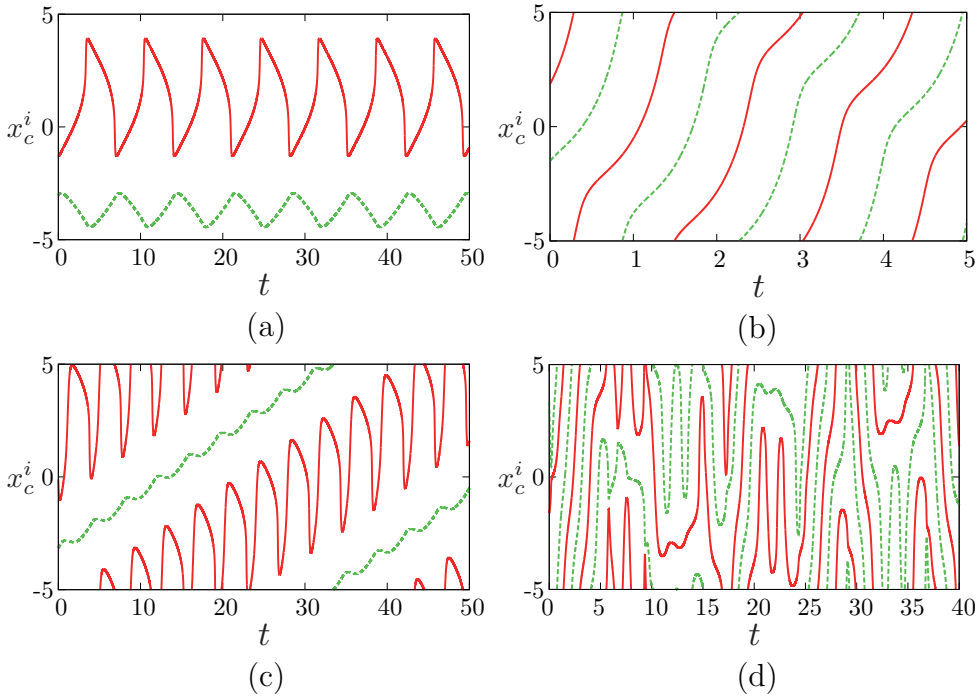

Figure 3: The trajectory of the asymptotic solution x_c^1 and x_c^2. (a) An asymmetric oscillatory solution ($\mu = 0.0196$). (b) A symmetric oscillatory rotating solution ($\mu = 0.00488$). (c) An asymmetric oscillatory solution ($\mu = 0.00179$). (d) An irregular motion solution ($\mu = 0.008$). All solutions are obtained by the numerical computation for (3) with $r = 0.5$, $L = 10$, $m = 2$ and $a = 0.05$.

Fig. 4(a), (b), (c) and (d) show typical example motions for solutions of Definition 1, 2, 3 and 4, respectively. These four types of solution can represent all the known characteristic motions of disks discovered in the previous researches [40, 41] except for irregular motions (Fig.3(d))

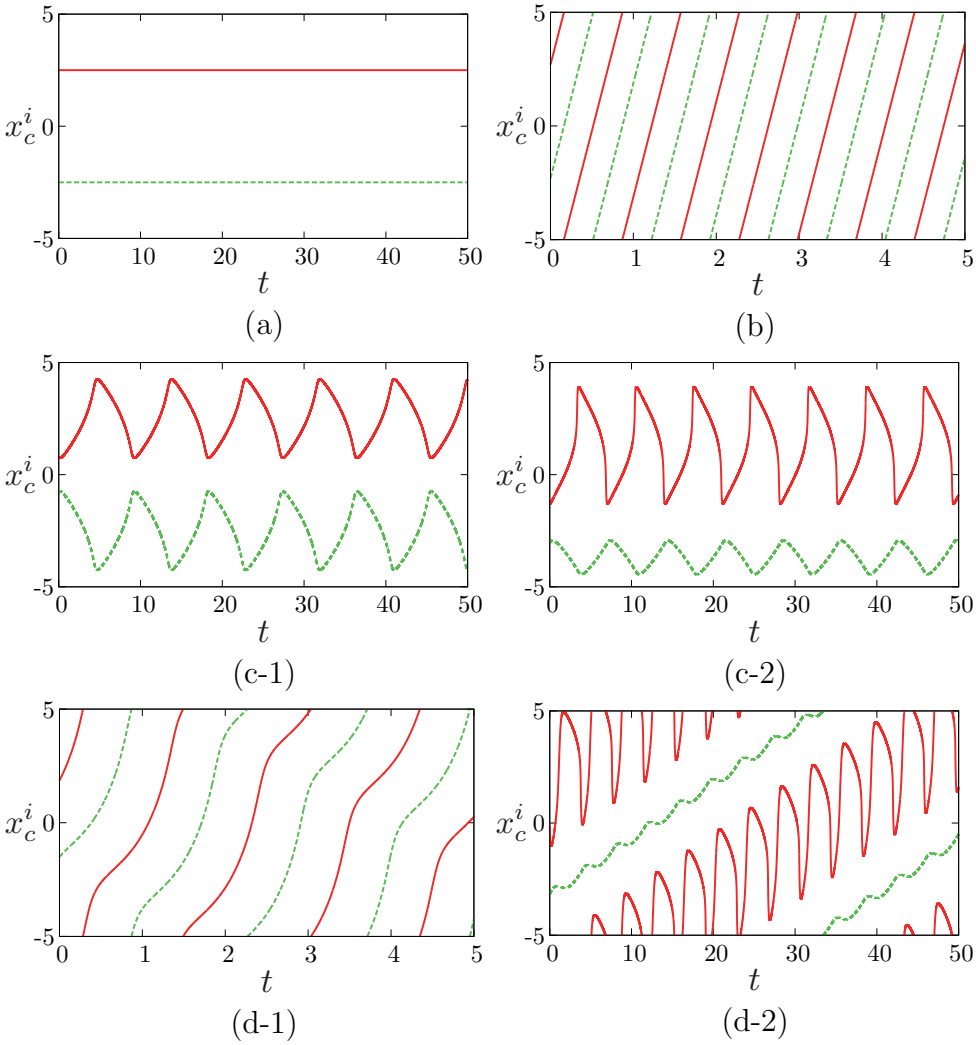

Figure 4: Plots of example motions (a), (b), (c) and (d) which correspond to solutions of Definition 1, 2, 3, and 4, respectively. (a) $\mu = 0.0202$, (b) $\mu = 0.00197$, (c-1) $\mu = 0.0198$, (c-2) $\mu = 0.0196$, (d-1) $\mu = 0.00488$, (d-2) $\mu = 0.0178$. The other parameters are $r = 0.5, L = 10, m = 2$ and $a = 0.05$

3 Numerical Results

Based on the definition explained in Chapter 3, we numerically analyzed the global bifurcation structure of (7).

3.1 Newfound motions and their definitions

In the previous researches [40, 41], only eight types of solution: symmetric motionless solution, symmetric/asymmetric rotating solution, symmet-

ric/asymmetric oscillatory solution, symmetric/asymmetric oscillatory rotating solution and irregular motion, have been reported, where the symmetries are about positions and amplitudes of disks for motionless/rotating solutions and oscillatory/oscillatory rotating solutions, respectively. As the result of our bifurcation analysis, we found another four types of motion: round-trip-asymmetric motion (Fig.5(a-2)), complete in-phase motion (Fig.5(b)), period-doubled motion (Fig.5(c-2)) and quasi-periodic motion (Fig.5(d-1)(d-2)). Round-trip-asymmetric motion is an oscillatory motion with different trajectories between the first and second half of its round-trip. In-phase motion is one of the periodic motions. Unlike the other motions, the disks oscillate in the same directions as shown in Fig.5(b). Period-doubled motion is a motion derived from a periodic motion. Although its trajectory is similar to the original one, there is a difference between the two successive periodic orbits. Its period is doubled from the original period because of the difference. Quasi-periodic motion has two different periods in its motion. In some figures, we negate constant rotating velocity by giving non-zero c for visibility.

From the observation of these motions, we introduce additional mathematical definitions of motion to classify them. In the following definitions, we fix $N = 2$ for simplicity. Note that domains of solutions defined in Chapter 2 can be extended to $\mathbb{R}$ since they are stationary or periodic solutions.

Definition 5 (Position-(a)symmetric solution)**.** *Suppose* (v, z_c^1, z_c^2, c) *is a motionless or rotating solution of* (7) *with* $N = 2$*. The solution is called a* position-symmetric solution *if*

$$|z_c^1(t) - z_c^2(t)| = L/2$$

holds for all $t > 0$*. If not, it is called a* position-asymmetric *solution.*

Fig.2(a) and (b) are examples of position-symmetric and asymmetric solutions, respectively.

Definition 6 (Amplitude-(a)symmetric solution)**.** *Suppose* (v, z_c^1, z_c^2, c, T) *is an oscillatory or oscillatory rotating solution of* (7) *with* $N = 2$*. The solution is called an* amplitude-symmetric solution *if*

$$\max_t z_c^1(t) - \min_t z_c^1(t) = \max_t z_c^2(t) - \min_t z_c^2(t)$$

holds. If not, it is called an amplitude-asymmetric *solution.*

Fig.4(c-1) and (c-2) are examples of an amplitude-symmetric and asymmetric solution, respectively.

Definition 7 (Round-trip-(a)symmetric oscillatory solution)**.** *Suppose* (v, z_c^1, z_c^2, c, T) *is an oscillatory solution of* (7) *with* $N = 2$*. The solution is called a* round-trip-symmetric oscillatory solution *if*

$$z_c^i(t) - z_c^i(0) = z_c^i(T/2) - z_c^i(t + T/2)$$

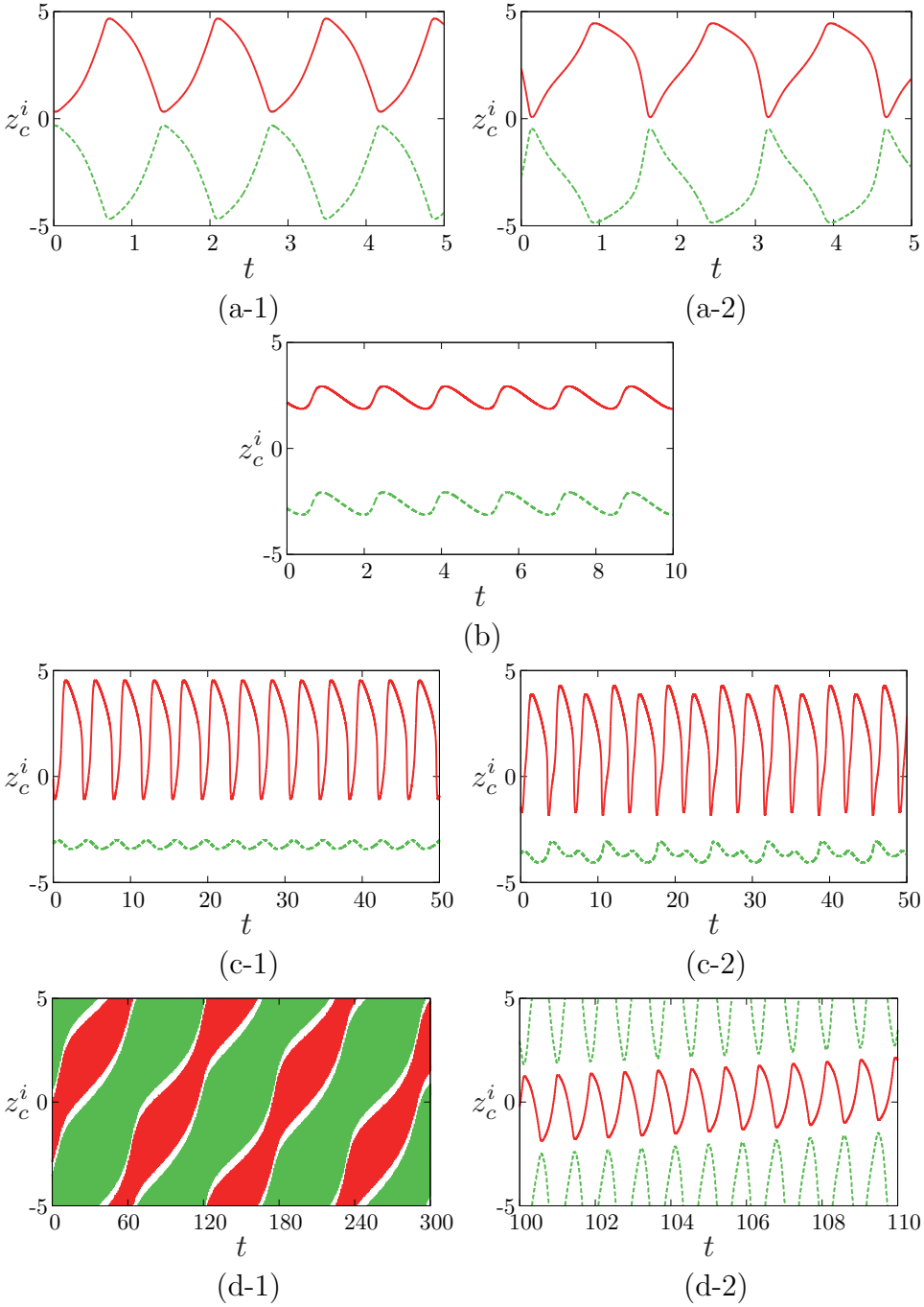

Figure 5: Plots of newfound motions with auxiliary plots for comparison. (a-1) Round-trip *symmetric* solution ($\mu = 0.00796, c = 0$). (a-2) Round-trip *asymmetric* solution ($\mu = 0.00801, c = 0$). (b) Complete in-phase solution ($\mu = 0.0149871, c = 2.8871$). (c-1) 1-period solution ($\mu = 0.0177824, c = 0.250286$). (c-2) 2-period solution ($\mu = 0.0158555, c = 0.517698$). (d-1) A quasi-periodic motion ($\mu = 0.0033, c = 0$). (d-2) A detailed figure of (d-1) ($100 \leq t \leq 110$).

holds for $i = 1, 2$ *and all* $t > 0$*. If not, it is called a* round-trip-asymmetric oscillatory solution.

The definition above means that the trajectory of the first half of their round-trip is equal to the inverted one of the second half. Fig.5(a-1) and (a-2) show example motions which correspond to a round-trip-symmetric and asymmetric solution, respectively. Note that we do not consider round-trip-symmetry on oscillatory *rotating* solutions because they are usually round-trip-asymmetric due to their constant rotating velocity.

Definition 8 (Complete in-phase solution)**.** *Suppose* (v, z_c^1, z_c^2, c, T) *is an oscillatory or oscillatory rotating solution of* (7) *with* $N = 2$*. The solution is called a* complete in-phase solution *if*

$$\underset{\theta\in[-T/2,T/2)}{\operatorname{argmin}} \int_0^T |\tilde{z}_c^1(t) - \tilde{z}_c^2(t+\theta)|dt = \{0\}.$$

holds.

Fig.5(b) shows an example motion which corresponds to a complete in-phase solution.

For clarity of explanation, we assign a symbol to each type of motion we found based on the following assignment table (Table 1). A sequence of letters combined along each row corresponds to each type of motion. We omit unnecessary letters for simplicity.

3.2 Bifurcation Diagram

We numerically obtained the bifurcation diagram in the case of $N = 2$ and $L = 10$ (Fig. 6), which is known as the parameter region where complicated solutions appear. Fig. 7 shows typical examples of all the types of motion we found. For visibility of period-doubling transitions, we added z_c^1-z_c^2 plots of 2^n-periodic solutions (Fig. 8).

Previously only limited parts of the bifurcation structure, stationary solution branches, were examined. This numerical bifurcation analysis revealed the structure among not only stationary solutions but periodic ones. Owing to that, we were able to make mainly five notable observations about periodic motions, including chaotic ones: (1) there are stable branches of OSA (round-trip-asymmetric motion) which is a newfound motion. (2) There is an OrSI (complete-in-phase motion, which is also newfound) branch which is not directly connected to any stable branches. (3) There is a complicated part of the bifurcation structure hidden by the stable branch of OrSN around $0.002 \leq \mu \leq 0.005$(Fig.9), which was not discovered in previous research even though it has some stable branches. (4) A bifurcation process that is probably a period-doubling cascade exists near $\mu = 0.016$ (Fig.10).

Table 1: Notation rules

Solution type	Period multiplier	Amp. sym.	Round-trip sym.	Complete-in-phase
Motionless L[1]	—	—	—	—
Rotating R[1]	—	—	—	—
Oscillatory O	(1-period)	Symmetric S	Symmetric S	(Not complete-in-phase)
			Asymmetric A	
		Asymmetric A	Symmetric S	
			Asymmetric A	
Oscillatory Rotating Or	(1-period)	Symmetric S	(Asymmetric)	Complete-in-phase I
				Not complete-in-phase N
		Asymmetric A		(Not complete-in-phase)
	N-period N	Asymmetric A		
Quasi-periodic Rotating Qpr	—	—	—	—

[1] All motionless/rotating solutions we found in this research are position-symmetric and the other characteristics are not applicable.

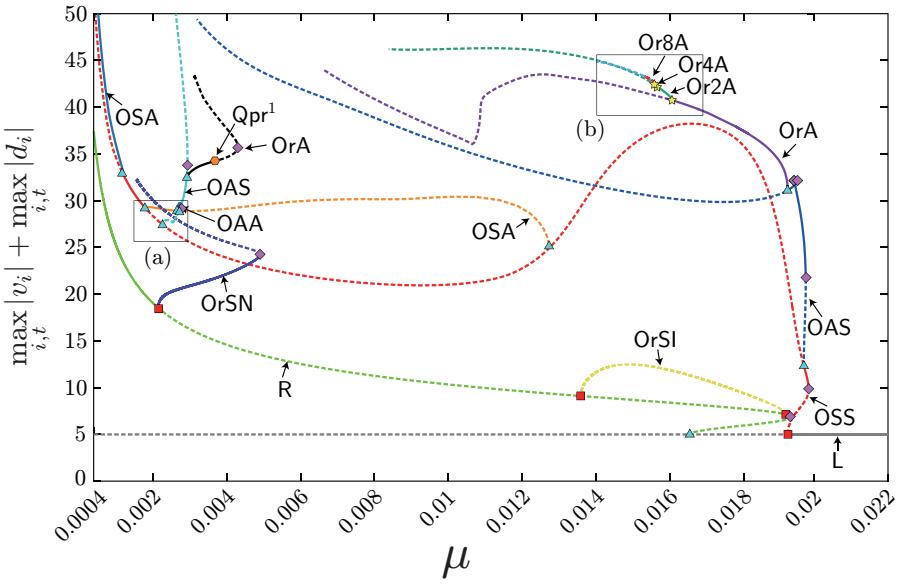

Figure 6: Bifurcation diagram obtained numerically for solutions defined in Chapter 2. The value of the Y-axis, where $d_i(t)$ and $v_i(t)$ represent the distance to the next disk of i-th disk and velocity on the original(stationary) coordinate system at time t, respectively, is defined to be able to separate each branch curve. Solid lines indicate stable solutions, whereas dashed lines indicate unstable solutions. Five types of bifurcation points: Hopf, pitchfork, saddle-node, period-doubling, and a torus are represented by a square, triangle, diamond, star ,and hexagon, respectively. Some branches disappear in the middle because the continuation of those branches was impossible due to their strong instability. [1]The branch of Qpr is not on this diagram because it does not match with Definition 1, 2, 3 or 4. However, we numerically obtained stable Qpr solutions (Fig.7(m-1) and (m-2)) near the torus bifurcation point by computing time evolution. Therefore, we state that there exists a branch of Qpr.

(5) A torus bifurcation point exists near $\mu = 0.004$. The last two observations can give us some hints of the mechanism whereby the chaotic motion emerges, which has never been discussed before even though it appears in a large portion of the parameter space. Thus we discuss the mechanism in the next chapter.

4 Analysis of the Chaotic Motion

Considering the bifurcation structures we obtained, there are two possible bifurcation routes to the chaotic motion via period-doubling bifurcation and torus one. Both have well-known mechanisms by which chaotic motions emerge: period-doubling cascade and torus breakdown [42, 43], respectively. In this section, we numerically compute the maximum Lyapunov exponent [44], which is an indicator of chaotic motion [42], and investigate

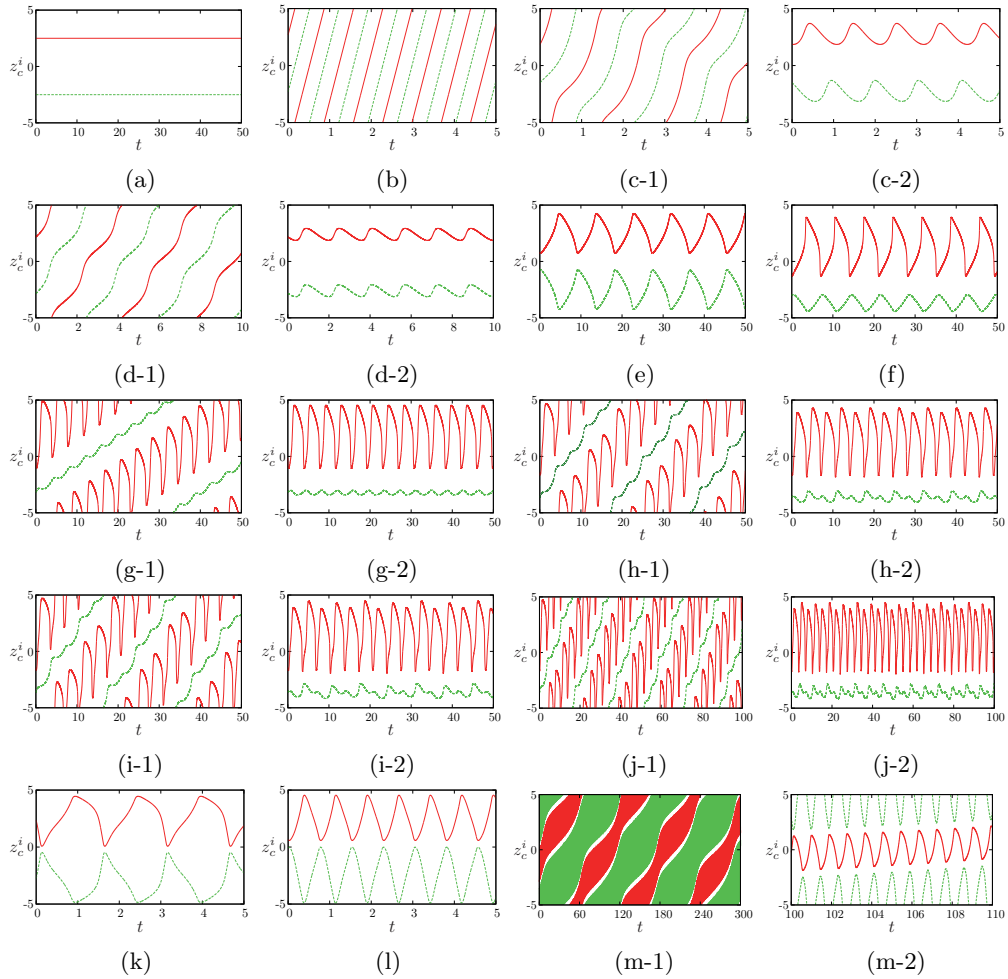

Figure 7: Plots of trajectories of all the motions found. (a) L ($c = 0, \mu = 0.0202$) (b) R ($c = 0, \mu = 0.00197$) (c-1)(c-2) OrSN ($\mu = 0.00488$) with $c = 0$ and $c = 7.58$ (resp.) (d-1)(d-2) OrSI ($\mu = 0.015$) with $c = 0$ and $c = 2.89$ (resp.) (e) OSS ($c = 0, \mu = 0.0198$) (f) OAS ($c = 0, \mu = 0.0196$) (g-1)(g-2) OrA ($\mu = 0.0179$) with $c = 0$ and $c = 0.25$ (resp.) (h-1)(h-2) Or2A ($\mu = 0.0159$) with $c = 0$ and $c = 0.518$ (resp.) (i-1)(i-2) Or4A ($\mu = 0.01559$) with $c = 0$ and $c = 0.548$ (resp.) (j-1)(j-2) Or8A ($\mu = 0.01558$) with $c = 0$ and $c = 0.549$ (resp.) (k) OSA ($c = 0, \mu = 0.00796$) (l) OAA($c = 0, \mu = 0.00275$) (m-1)(m-2) Qpr ($\mu = 0.0033, c = 0$) in $0 \leq t \leq 300$ and $100 \leq t \leq 110$ (resp.)

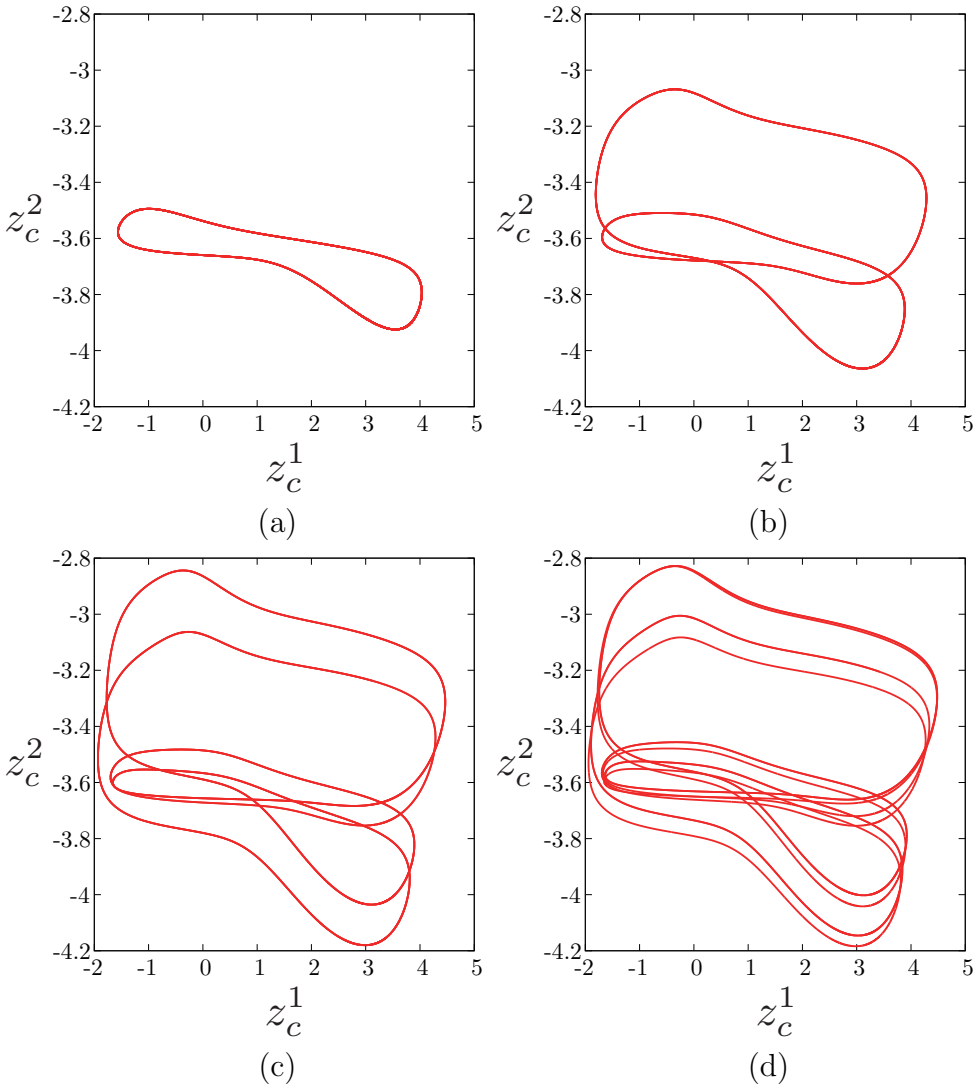

Figure 8: z_c^1-z_c^2 plots for (a)OrA($\mu = 0.0179, c = 0.25$), (b)Or2A($\mu = 0.0159, c = 0.518$), (c)Or4A($\mu = 0.01559, c = 0.548$) and (d)Or8A($\mu = 0.01558, c = 0.549$).

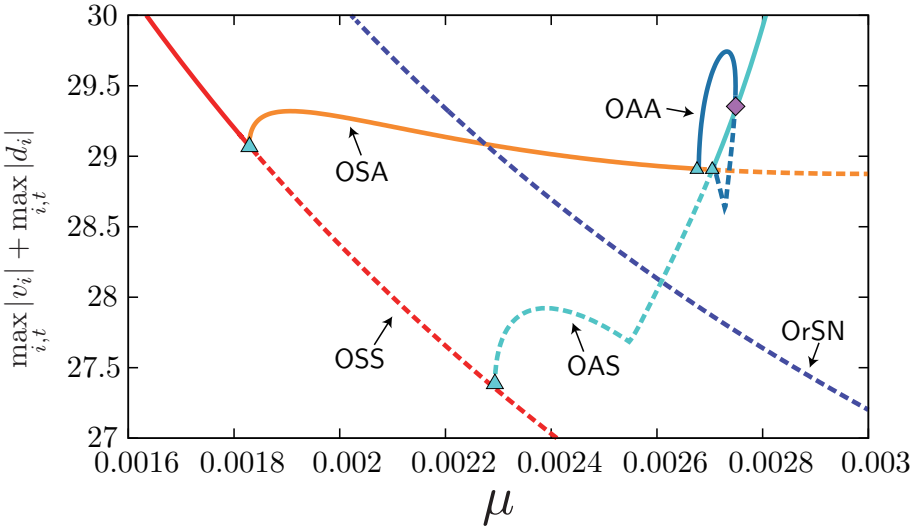

Figure 9: A detailed figure of Fig.6 (a).

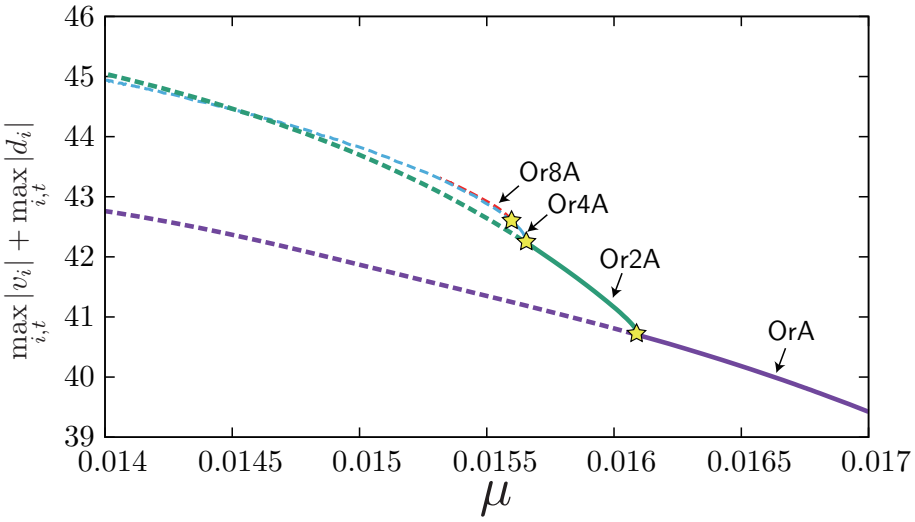

Figure 10: A detailed figure of Fig.6 (b).

the relationship between those two bifurcation processes and chaotic motion in this system. Fig.11 shows that both ends of the parameter region where chaotic motions in terms of Lyapunov exponent occur, that is, the region where the maximum Lyapunov exponent is positive, coincide with the parameters where the period-doubling bifurcations repeatedly occur, and the saddle-node bifurcation point of the stable OrSN branch lies. The coincidence at the right side of the region (near $\mu = 0.016$) implies that the repeated period-doubling bifurcations are most likely to be a part of the period-doubling cascade, which leads to chaos. In addition, oscillatory and oscillatory rotating solutions sporadically exist around $0.014 \leq \mu \leq 0.016$, which are likely to be periodic windows, which are incidental to period-doubling cascade. Fig.12 shows trajectories of periodic solutions found in the periodic windows. Moreover, chaotic attractors [42] are likely to exist near the period-doubling cascade (Fig.13). The left end of the chaotic region coincides with the saddle-node point of the OrSN branch, and the transition from OrSN to chaos occurs suddenly according to the very sharp change of the maximum Lyapunov exponent. Our bifurcation analysis can be explained as follows: there should exist a torus breakdown point that emerges from the torus bifurcation point near $\mu = 0.004$. That should lead to chaos, however, the basin of the stable OrSN is so large that usual numerical calculations result in converging to OrSN solutions quickly(Fig.14), which is the possible reason why chaotic behaviors suddenly appear after the OrSN branch disappears at the saddle-node point.

5 Conclusion

This study clarifies the motion of two camphor disks in an annular water channel by numerical bifurcation calculations for the particle reaction-diffusion model under periodic boundary conditions. As a result, we were able to find new stable solutions (the round-trip-asymmetric solution, N-period solution ($N = 2, 4, 8$), and quasi-periodic solution) that could not be found in previous studies. In addition, the numerical calculation of the maximum Lyapunov exponent showed that the motion shown as irregular motion in the previous result [41] is chaotic motion. The mathematical analysis of our model of the two self-propelled materials is limited to the existence of motionless, rotating, and asymmetric rotating solutions. Therefore, we want to analyze the existence and stability of periodic solutions in the future.

A Discretization

In order to numerically analyze the bifurcation structure of (7), we need to discretize the system. It is preferable to employ Fourier series expansion rather than naive finite-difference method for discretization of $v(z, t)$

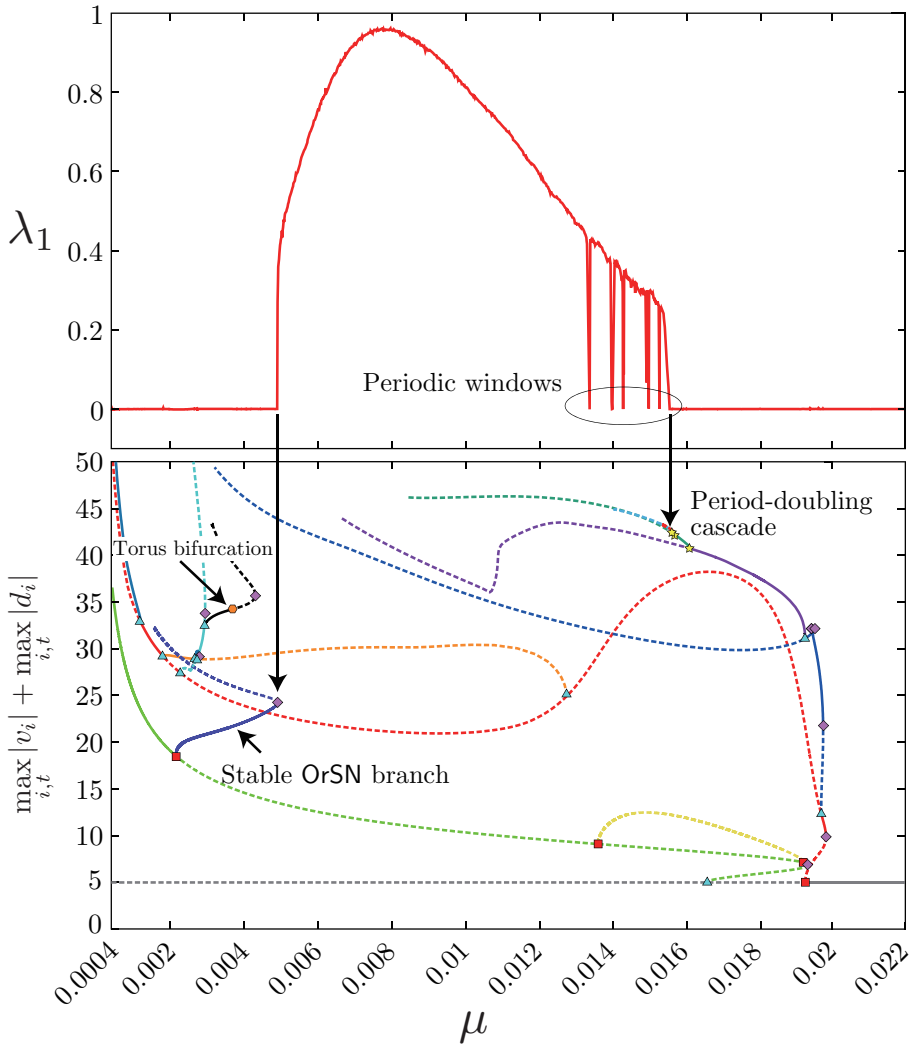

Figure 11: Plot of maximum Lyapunov exponent λ_1 coupled with the bifurcation diagram.

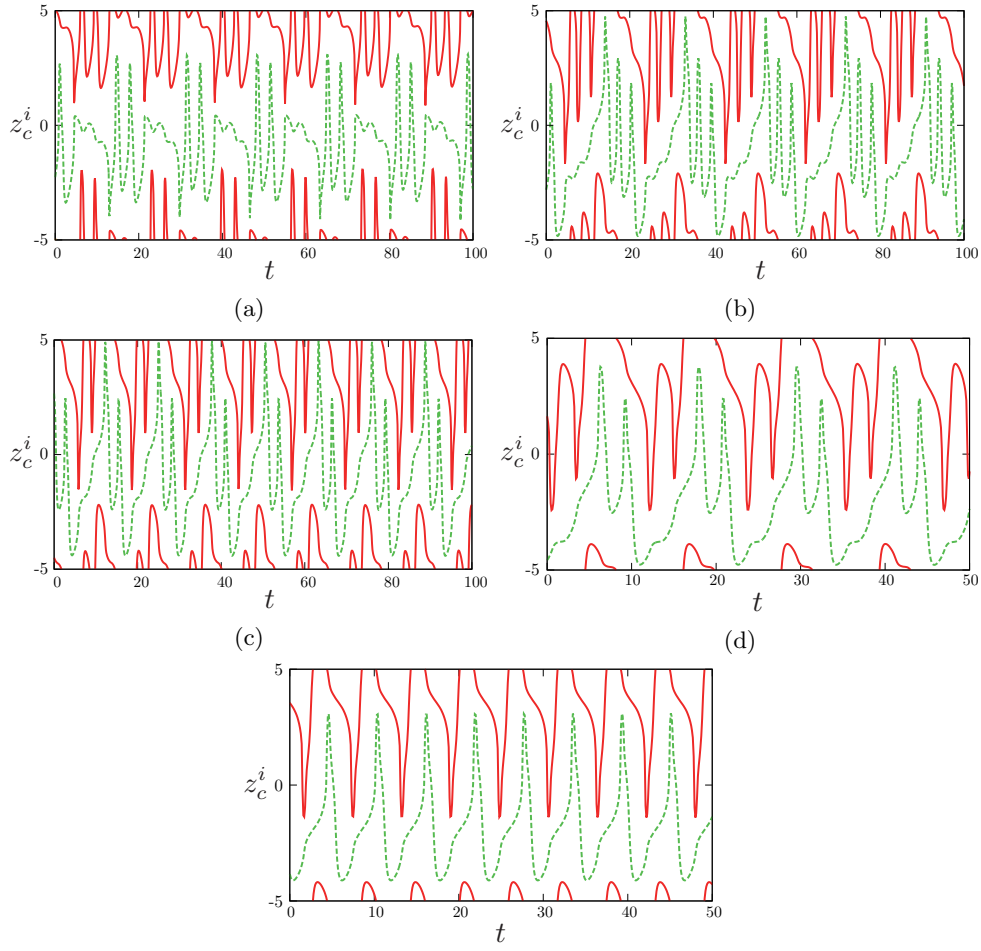

Figure 12: Plots of periodic solutions found in the periodic windows (a) $\mu = 0.01531, c = 0.29$, (b) $\mu = 0.01502, c = 0$, (c) $\mu = 0.01432, c = -0.012$, (d) $\mu = 0.01402, c = 0.021$, (e) $\mu = 0.01341, c = 0$.

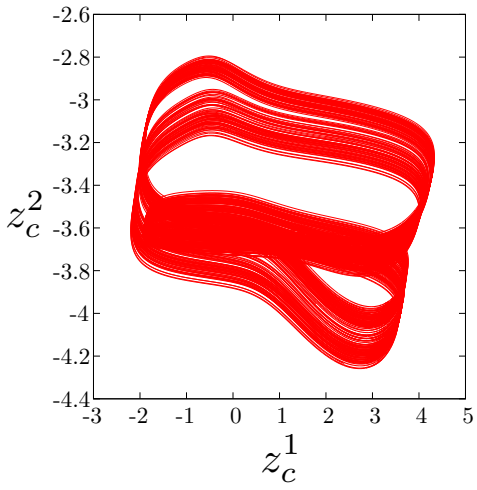

Figure 13: A plot of a trajectory that is likely to be on a chaotic attractor near the period doubling cascade.($\mu = 0.015577, c = 0.550517$)

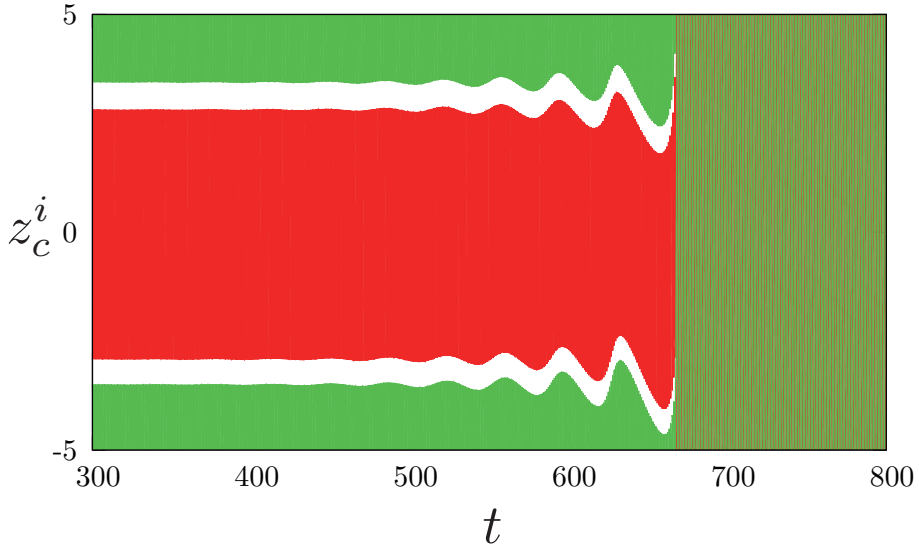

Figure 14: A failed transition to a quasi-periodic solution that resulted in falling onto OrSNN ($\mu = 0.00347, c = 0.16$)

.

because the term $v(\pi_L(z_c^i \pm r), t)$ may require values of v on arbitrary points in $[-L/2, L/2)$.

Let $(Z_c^1(t), ..., Z_c^N(t))$ be the positions of disks in the discretized system. Let us define a function $V : \mathbb{R}^2 \to \mathbb{R}$ as follows:

$$V(z,t) = \frac{a_0(t)}{2} + \sum_{k=1}^{M} \left(a_k(t) \cos\left(\frac{2\pi k z}{L}\right) + b_k(t) \sin\left(\frac{2\pi k z}{L}\right) \right),$$

which represents v in the form of truncated Fourier series with wave number M and real coefficients $(a_0(t), a_1(t), ..., a_M(t), b_1(t), ..., b_M(t))$. In the following, we obtain the discretized system of (7), that is, the set of ordinary differential equations between $(Z_c^1(t), ..., Z_c^N(t))$ and $(a_0(t), a_1(t), ..., a_M(t), b_1(t), ..., b_M(t))$.

First, we substitute v and z_c^i in (7) with V and Z_c^i. Then, we obtain

$$\begin{aligned} \mu \frac{dZ_c^i}{dt} &= \frac{\gamma(V(\pi_L(Z_c^i + r), t)) - \gamma(V(\pi_L(Z_c^i - r), t))}{2r} - \mu c \quad (i = 1, ..., N), \\ \frac{\partial V}{\partial t} &= \frac{\partial^2 V}{\partial z^2} - c\frac{\partial V}{\partial z} - V + \sum_{i=1}^{N} F(z - Z_c^i). \end{aligned} \tag{8}$$

The left-hand side of the second equation is

$$\frac{\partial V}{\partial t} = \frac{1}{2}\frac{da_0}{dt} + \sum_{k=1}^{M} \left(\frac{da_k}{dt} \cos\left(\frac{2\pi k z}{L}\right) + \frac{db_k}{dt} \sin\left(\frac{2\pi k z}{L}\right) \right).$$

The right-hand side is

$$
\begin{aligned}
&\frac{\partial^2 V}{\partial z^2} - c\frac{\partial V}{\partial z} - V + \sum_{i=1}^{N} F(z - Z_c^i) \\
=&\sum_{k=1}^{M}\left\{-\left(\frac{2\pi k}{L}\right)^2 a_k \cos\left(\frac{2\pi kz}{L}\right) - \left(\frac{2\pi k}{L}\right)^2 b_k \sin\left(\frac{2\pi kz}{L}\right)\right\} \\
&+\sum_{k=1}^{M}\left\{-\frac{2\pi kc}{L} a_k \sin\left(\frac{2\pi kz}{L}\right) + \frac{2\pi kc}{L} b_k \cos\left(\frac{2\pi kz}{L}\right)\right\} \\
&-\left\{\frac{1}{2}a_0 + \sum_{k=1}^{M}\left(a_k \cos\left(\frac{2\pi kz}{L}\right) + b_k \sin\left(\frac{2\pi kz}{L}\right)\right)\right\} \\
&+\sum_{i=1}^{N} F(z - Z_c^i) \\
=&-\frac{1}{2}a_0 \\
&+\sum_{k=1}^{M}\left\{c_k \cos\left(\frac{2\pi kz}{L}\right) + d_k \sin\left(\frac{2\pi kz}{L}\right)\right\} \\
&+\sum_{i=1}^{N} F(z - Z_c^i)
\end{aligned}
$$

where

$$
c_k(t) = -\left\{\left(\frac{2\pi k}{L}\right)^2 + 1\right\} a_k(t) + \frac{2\pi kc}{L} b_k(t)
$$

and

$$
d_k(t) = -\frac{2\pi kc}{L} a_k(t) - \left\{\left(\frac{2\pi k}{L}\right)^2 + 1\right\} b_k(t)
$$

for $k = 1, ..., M$. Note that here F is

$$
F(x) = \begin{cases} 1, & |x| \le r, \\ 0, & |x| > r. \end{cases}
$$

Next, let us integrate both sides from $z = -L/2$ to $L/2$ then we obtain

$$
\frac{L}{2}\frac{da_0}{dt} = -\frac{L}{2}a_0 + 2Nr.
$$

Similarly, we multiply $2\cos(2\pi kz/L)/L$ on both sides and integrate them from $z=-L/2$ to $L/2$ then the following is obtained:

$$\begin{aligned}&\frac{da_k}{dt}\\ =&c_k+\frac{1}{k\pi}\sum_{i=1}^{N}\left\{\sin\left(\frac{2\pi k(Z_c^i+r)}{L}\right)-\sin\left(\frac{2\pi k(Z_c^i-r)}{L}\right)\right\}\\ =&c_k+\frac{2}{k\pi}\sin\left(\frac{2\pi kr}{L}\right)\sum_{i=1}^{N}\cos\left(\frac{2\pi kZ_c^i}{L}\right)\end{aligned}$$

for $k=1,...,M$. For b_k, we multiply $2\sin(2\pi kz/L)/L$ on both sides and integrate them from $z=-L/2$ to $L/2$ then the following is obtained:

$$\begin{aligned}&\frac{db_k}{dt}\\ =&d_k-\frac{1}{k\pi}\sum_{i=1}^{N}\left\{\cos\left(\frac{2\pi k(Z_c^i+r)}{L}\right)-\cos\left(\frac{2\pi k(Z_c^i-r)}{L}\right)\right\}\\ =&d_k+\frac{2}{k\pi}\sin\left(\frac{2\pi kr}{L}\right)\sum_{i=1}^{N}\sin\left(\frac{2\pi kZ_c^i}{L}\right).\end{aligned}$$

for $k=1,...,M$. To sum up, we obtained

$$\begin{cases}\dfrac{da_0}{dt} &= -a_0+\dfrac{4Nr}{L},\\ \dfrac{da_k}{dt} &= c_k+\dfrac{2}{k\pi}\sin\left(\dfrac{2\pi kr}{L}\right)\displaystyle\sum_{i=1}^{N}\cos\left(\dfrac{2\pi kZ_c^i}{L}\right),\\ \dfrac{db_k}{dt} &= d_k+\dfrac{2}{k\pi}\sin\left(\dfrac{2\pi kr}{L}\right)\displaystyle\sum_{i=1}^{N}\sin\left(\dfrac{2\pi kZ_c^i}{L}\right),\\ k=1,...,M.\end{cases}$$

Combining the first equation of (8), the discretized system of (8) to be obtained is

$$\begin{cases}\dfrac{da_0}{dt} &= -a_0+\dfrac{4Nr}{L},\\ \dfrac{da_k}{dt} &= c_k+\dfrac{2}{k\pi}\sin\left(\dfrac{2\pi kr}{L}\right)\displaystyle\sum_{i=1}^{N}\cos\left(\dfrac{2\pi kZ_c^i}{L}\right),\\ \dfrac{db_k}{dt} &= d_k+\dfrac{2}{k\pi}\sin\left(\dfrac{2\pi kr}{L}\right)\displaystyle\sum_{i=1}^{N}\sin\left(\dfrac{2\pi kZ_c^i}{L}\right),\\ \mu\dfrac{dZ_c^i}{dt} &= \dfrac{\gamma(V(\pi_L(Z_c^i+r),t)-\gamma(V(\pi_L(Z_c^i-r),t))}{2r}-\mu c,\\ k=1,...,M,\quad i=1,...,N\end{cases}\tag{9}$$

where

$$V(z,t) = \frac{a_0(t)}{2} + \sum_{k=1}^{M} \left(a_k(t) \cos\left(\frac{2\pi kz}{L}\right) + b_k(t) \sin\left(\frac{2\pi kz}{L}\right) \right),$$

$$c_k(t) = -\left\{ \left(\frac{2\pi k}{L}\right)^2 + 1 \right\} a_k(t) + \frac{2\pi kc}{L} b_k(t),$$

$$d_k(t) = -\frac{2\pi kc}{L} a_k(t) - \left\{ \left(\frac{2\pi k}{L}\right)^2 + 1 \right\} b_k(t).$$

Typically we used $M = 128$ in this paper.

B Numerical methods

For solving the discretized system (9), we employed a four-stage fourth-order L-stable Rosenbrock method called ROS4 [46] by E. Hairer and G. Wanner [49]. Pseudoarclength continuation method [50] was used for branch continuation. To find periodic solutions, we employed Newton Shooting Method [54]. To compute eigenvalues and eigenvectors, we used ARPACK [53] for sparse matrices and the routine implemented in Eigen 3.3.9 [51] which is based on EISPACK [52] for dense matrices.

B.1 Time integration

It is essential to choose a time integration method that works effectively in terms of computation time since time integration accounts for a large part of the computation time in finding periodic solutions, which is typically quite long. The basic idea is to choose an adaptive time step method [48, 49]. Profiles of periodic solutions in the system (7) ($N = 2$) typically quickly change when the two disks get very close. This phenomenon occurs in a bit of time, and such quick changes do not occur in most of the period time,, which means that if we chose a fixed time-step method, we would have to take a tiny time step only for the moment of the quick change to be calculated stably and accurately. By choosing an adaptive time step method, we can employ a suitable step size most of the time and a small step size only when quick changes happen. (Fig. 15)

However, there is a factor that prevents the adaptive method from employing such well-optimized time step sizes, that is, the stiffness [49]. The discretized system (9) has coefficients in the order of $O(k^2)$, which can cause stiffness problems where step sizes become unreasonably small [49]. To avoid that, we need implicitness in the adaptive method we choose. There are many variants of (semi-)implicit adaptive method, so we decided to choose

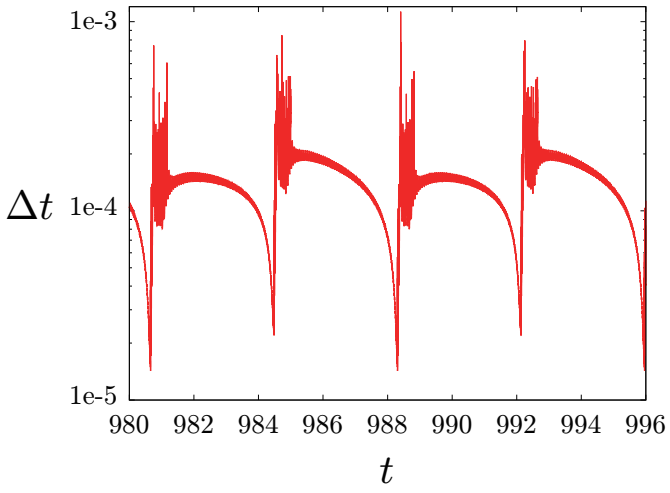

Figure 15: Adaptive change of Δt by ROS4. ($\mu = 0.016$) Decreasing spikes which indicate that very quick changes happen are observed.

one developed and implemented by E. Hairer and G. Wanner [47] because their methods and program codes have been well tested and reviewed by many users. Considering the balance between computational cost, stability and accuracy, we chose ROS4 [46], which performed well enough for our research purposes.

B.2 Pseudoarclength Method

The pseudoarclength method is a numerical continuation method introduced by H. B. Keller [50]. First, let us explain a very basic idea of numerical continuation (Fig.16). Let $\boldsymbol{F}(\boldsymbol{v}, \lambda)$ be a function that maps $\mathbb{R}^N \times \mathbb{R}$ to $\mathbb{R}^N$, where $\boldsymbol{v} \in \mathbb{R}^N$ and $\lambda \in \mathbb{R}$ are a set of arguments and a parameter in the function, respectively. Suppose that we want to track the branch defined by $\boldsymbol{F}(\boldsymbol{v}, \lambda) = \boldsymbol{0}$. Let $(\boldsymbol{v}_0, \lambda_0)$ be the first known point on the branch. To obtain the next point on the branch, we can apply Newton's method with a slightly shifted parameter λ_1. The initial data can be $\boldsymbol{v}_0$. In many situations, this attempt succeeds and results in the next point $(\boldsymbol{v}_1, \lambda_1)$ being obtained. We can repeat this process until we meet a saddle-node point such as the point with $\lambda = \lambda_s$. With this basic method, we cannot turn around the saddle-node point because if we let the new parameter be larger than λ_s, Newton's method would fail due to the nonexistence of solutions, or if we let it be smaller, the next point would stay on the solid line part.

Pseudoarclength method solves this problem (Fig.17). In the previous method, we shift the parameter along the parameter axis and let the solutions converge onto the branch perpendicularly to the parameter axis. The idea of pseudoarclength method is to do that on the tangent line axis. Let

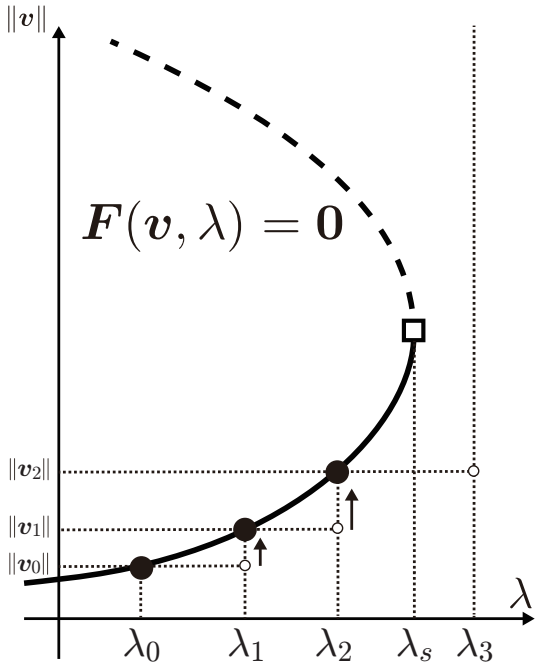

Figure 16: Schematic diagram of natural continuation.

$(\boldsymbol{v}_0, \lambda_0)$ be the first known point again. In addition, suppose that we know the unit tangent vector $(\dot{\boldsymbol{v}}_0, \dot{\lambda}_0)$ on the point. For the first step, they can be $(\boldsymbol{0}, 1)$ if the point is far from saddle-node points. We add a condition for Netwon's method to converge perpendicularly to the tangent line axis:

$$K(\boldsymbol{v}, \lambda; \Delta s) = \dot{\boldsymbol{v}}_0 \cdot (\boldsymbol{v} - \boldsymbol{v}_0) + \dot{\lambda}_0 \cdot (\lambda - \lambda_0) - \Delta s = 0$$

where Δs is a small shift along the axis. By solving

$$\begin{cases} \boldsymbol{F}(\boldsymbol{v}, \lambda) = \boldsymbol{0}, \\ K(\boldsymbol{v}, \lambda; \Delta s) = 0 \end{cases} \tag{10}$$

with Newton's method using the initial data $\tilde{\boldsymbol{v}}_1^0 = \boldsymbol{v}_0 + \dot{\boldsymbol{v}}_0 \Delta s$, $\tilde{\lambda}_1^0 = \lambda_0 + \dot{\lambda}_0 \Delta s$, we obtain the next point $(\boldsymbol{v}_1, \lambda_1)$. Here, let us calculate the unit tangent vector on $(\boldsymbol{v}_1, \lambda_1)$. The solution of (10) is considered to be parameterized by Δs. By taking derivative of (10) with respect to Δs on $(\boldsymbol{v}_1, \lambda_1)$, we obtain

$$\begin{pmatrix} \boldsymbol{F}_{\boldsymbol{v}}(\boldsymbol{v}_1, \lambda_1) & \boldsymbol{F}_{\lambda}(\boldsymbol{v}_1, \lambda_1) \\ \dot{\boldsymbol{v}}_0{}^T & \dot{\lambda}_0 \end{pmatrix} \begin{pmatrix} \dot{\boldsymbol{v}}_1 \\ \dot{\lambda}_1 \end{pmatrix} = \begin{pmatrix} \boldsymbol{0} \\ 1 \end{pmatrix} \tag{11}$$

The unit tangent vector on $(\boldsymbol{v}_1, \lambda_1)$ is obtained by solving (11) for $(\dot{\boldsymbol{v}}_1, \dot{\lambda}_1)$ and normalizing it. Then, let us renew the tangent line axis and repeat this process. Using this method, we can turn around the saddle-node point as described in Fig.17.

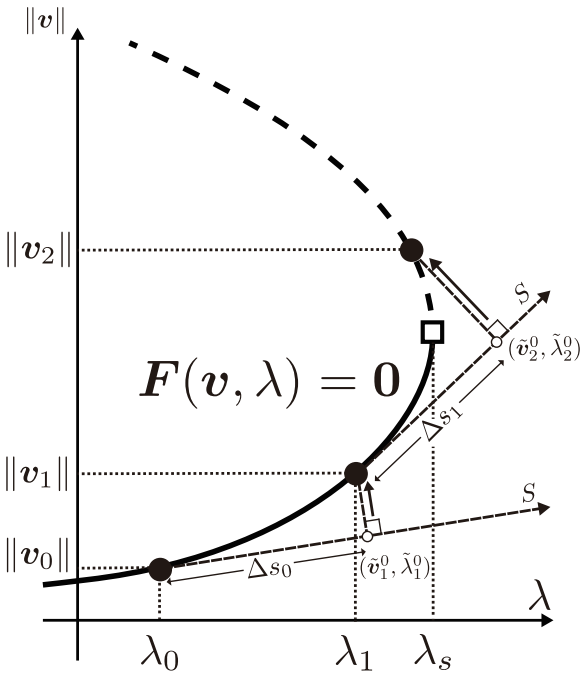

Figure 17: Schematic diagram of pseudoarclength continuation.

B.3 Calculation of Jacobian Matrix

In the computation of implicit time integration and Newton method, we need to solve a linear problem in the form of $\mathbf{D}\boldsymbol{F}(\boldsymbol{p})\boldsymbol{x}=\boldsymbol{b}$ where $\mathbf{D}\boldsymbol{F}(\boldsymbol{p})$ is the Jacobian matrix of $\boldsymbol{F}:\mathbb{R}^N\to\mathbb{R}^N$ on $\boldsymbol{p}$. There are mainly three possible ways to obtain the Jacobian matrix in numerical computation:

1. Finite difference method.
2. Analytic derivative.
3. Automatic differentiation [55].

The first one is a very basic numerical method: approximately give the i-th column of $\mathbf{D}\boldsymbol{F}(\boldsymbol{p})$ by a finite difference $(\boldsymbol{F}(\boldsymbol{p}+\sigma\boldsymbol{e}_i)-\boldsymbol{F}(\boldsymbol{p}))/\sigma$ (or higher-order one) where $\boldsymbol{e}_i$ is the i-th natural basis and σ is a small perturbation size. This method can be used in various situations even if the explicit form of $\boldsymbol{F}$ is unknown. However, this approximation inherently contains some error, especially when the perturbation size σ is not optimized well. The second one gives us a very accurate result. However, correctly calculating analytic derivatives can be unreasonably complicated hard work in some cases. The third one is useful when we need accuracy without any additional analytic calculation. We employed the third method for the accuracy and correctness of derivative calculations and the finite difference method if applicable.

References

[1] T. Vicsek, A. Czirok, E. Ben-Jacob, I. Cohen, O. Shochet, *Novel type of phase transition in a system of self-driven particles*, Phys. Rev. Lett.75, 1226–1229 (1995).

[2] M. Ballerini, N. Cabibbo,R. Candelier, A. Cavagna, E. Cisbani, I. Giardina et al. , *Interaction ruling animal collective behavior depends on topological rather than metric distance: evidence from a field study*, Proc. Natl. Acad. Sci. USA 105, 1232–1237 (2008).

[3] J. K. Parrish and L. Edelstein-Keshet, *Complexity, Pattern, and Evolutionary Trade-Offs in Animal Aggregation*, Science 284, 99-101(1999).

[4] J. Buhl, D. J. T. Sumpter, I. D. Couzin, J. J. Hale, E. Despland, E. R. Miller, S. J. Simpson, *From disorder to order in marching locusts*, Science 312, 1402-1406 (2006).

[5] E. Méhes and T. Vicesk, *Collective motion of cells: from experiments to models* Integr. Biol. 6, 831-854 (2014).

[6] N. Shimoyama, T. Mizuguchi, Y. Hayakawa and M. Sano. *Collective Motion in a System of Motile Elements*, Phys. Rev. Lett., 76(20),)2870-3873 (1996).

[7] J. Toner and Y. Tu, *Flocks, herds, and schools: A quantitative theory of flocking* , Phys. Rev. R 58(4), 4828- 4858 (1998).

[8] A. Czirók and T. Vicsek, *Collective behavior of interacting self-propelled particles*, Physica A, 281, 17-29 (2000).

[9] H. Kevine, W.-J. Pappel and I. Cohenm *Self-organization in systems of self-propelled particles* , Phys. Rev. E, 63, 017101 (200).

[10] T. Niisato and Y.-P. Gunji, *Metric-topological interaction model of collective behavior*, Ecological Modelling, 222, 3041-3049 (2011).

[11] H. .E. Ribeiro and F. Q. Potiguar, *Active matter in lateral parabolic confinement: From subdiffusion to superdiffusion*, Physica A, 462, 1294-1300 (2016).

[12] A. .E. B. T. King and M. S. Tumerm *Non-local interactions in collective motion*, R. .Soc. Open Sci., 8, 201536 (2021).

[13] T. Sanchez,D. T. Chen, S. J. Decamp, M. Heymann and Z. Dogic, *Spontaneous motion in hierarchically assembled active matter*, Nature 491, 431-434 (2012).

[14] Y. Hong, D. Velegol, N. Chatuvedi and A. Sen, *Biomimetic behavior of synthetic particles: from microscopic randomness to macroscopic control*, Phys. Chem. Chem. Phys., 23, 1423-1435 (2010).

[15] Y. Sumino, K. H. Nagai, Y. Shitaka, D. Tanaka, K. Yoshikawa, H. Chaté, K. Oiwa, *Large-scale vortex lattice emerging from collectively moving microtubules*, Nature 483, 448-452 (2012).

[16] N. Kumar, H. Soni, S. Ramaswamy and A. K. Sood, *Flocking at a distance in active granular matter*, Nature Communications 5, 4688 (2014).

[17] H. R. Jiang, N. Yoshinaga, M. Sano, Active Motion of a Janus Particle by Self-Thermophoresis in a Defocused Laser Beam, Phys. Rev. Lett. 105 (2010) 268302.

[18] I. Buttinoni, J. Bialké, F. Kùmmel, H. Lòwen, C. Bechinger, T. Speck, *Dynamical clustering and phase separation in suspensions of self- propelled colloidal particles*, Phys. Rev. Lett. 110, 1-8 (2013).

[19] S. Nakata, Y. Iguchi, S. Ose, M. Kuboyama,T. Ishii and K. Yoshikawa, *Self-Rotation of a Camphor Scraping on Water; New Insight into the Old Problem*, Langmuir 13, 4454 (1997).

[20] Y. Sumino, N. Magome, T. Hamada and K. Yoshikawa, *Self-Running Droplet: Emergence of Regular Motion from Nonequilibrium Noise*, Phys. Rev. Lett., 94, 068301 (2005).

[21] K. Nagai, Y. Sumino, H. Kitahata, and K. Yoshikawa, *Mode selection in the spontaneous motion of an alcohol droplet*, Phys. Rev. E ,71, 065301(R) (2005).

[22] N. J. Suematsu, S. Nakata, A. Awazu and H. Nishimori, *Collective behavior of inanimate boats*, Phys. Rev. E, 81, 056210 (2010).

[23] E. Heisler, N. J. Suematsu, A. Awazu, and H. Nishimori, *Swarming of self-propelled camphor boats,* Phys. Rev. E, 85, 055201(R) (2012).

[24] S. Soh, K. J. M. Bishop and B. A. Grzybowski *Dynamic Self-Assembly in Ensembles of Camphor Boats*, J. Phys. Chem. B, 112, 10848–10853 (2008).

[25] S. Soh, M. Branicki and B. A. Grzybowski, *Swarming in Shallow Waters*, J. Phys. Chem. Lett., 2, 770–774 (2011).

[26] N. J. Suematsu, K. Tateno, S. Nakata, H. Nishimori, *Synchronized Intermittent Motion Induced by the Interaction between Camphor Disks*, J. Phys. Soc. Jpn., 84, 034802 (2015).

[27] S. Tanaka, S. Nakata and T. Kano, *Dynamic ordering in a swarm of floating droplets driven by solutal Marangoni effect*, J. Phys. Soc. Jpn., 86, 101004 (2017).

[28] E. Heisler, N. J. Suematsu, A. Awazu, and H. Nishimori, *Collective Motion and Phase Transitions of Symmetric Camphor Boats*, J. Phys. Soc. Jpn., 81, 074605 (2012).

[29] Y. Matsuda, K. Ikeda, Y. S. Ikura, H. Nishimori and N. J. Suematsu, *Dynamical Quorum Sensing in Non-Living Active Matter*, J. Phys. Soc. Jpn., 88, 093002 (2019)

[30] M. Kim, M. Okamoto, Y. Yasugahira, S. Tanaka, S. Nakata, Y. Kobayashi and M. Nagayama, *A reaction-diffusion particle model for clustering of self-propelled oil droplets on a surfactant solution*, Physica D, 425, 132949(2021).

[31] S. Nakata, M. Nagayama, H. Kitahata, N. J. Suematsu, T. Hasegawa, *Physicochemical design and analysis of self-propelled objects that are characteristically sensitive to environments*, Phys. Chem. Chem. Phys., 17, 10326–10338 (2015),

[32] M. Nagayama, S. Nakata, Y. Doi and Y. Hayashima, *A theoretical and experimental study on the unidirectional motion of a camphor disk*, Physica D, 194, 151–165 (2004).

[33] Y. Koyano, N. Yoshinaga, and H. Kitahata, *General criteria for determining rotation or oscillation in a two-dimensional axisymmetric system*, J. Chem. Phys., 143, 014117/1-6 (2015).

[34] Y. Koyano, T. Sakurai, and H. Kitahata, *Oscillatory motion of a camphor grain in a one-dimensional finite region*, Phys. Rev. E, 94, 042215 (2016).

[35] Y. Koyano, N. J. Suematsu, and H. Kitahata, *Rotational motion of a camphor disk in a circular region*, Phys. Rev. E, 99, 022211 (2019).

[36] D. Boniface, C. Cottin-Bizonne, R. Kervil, C. Ybert, and F. Detcheverry, *Self-propulsion of symmetric chemically active particles: Point-source model and experiments on camphor disks*, Phys. Rev. E, 99, 062605 (2019).

[37] M. Okamoto, T. Gotoda, and M. Nagayama, *Global existence of a unique solution and a bimodal travelling wave solution for the 1D particle-reaction-diffusion system*, J. Phys. Commun., 5, 055016 (2021).

[38] M. Okamoto, T. Gotoda and M. Nagayama, *Existence and non-existence of asymmetrically rotating solutions to a mathematical model*

of self-propelled motion, Japan J. Indust. Appl. Math., 37(3), 883-912 (2020).

[39] J. Fan, M. Nagayama, G. Nakamura, M. Okamoto, *A weak solution for a point mass camphor motion*, Differential Integral Equations 33(7-8), 431-443 (2020).

[40] Y. S. Ikura, E. Heisler, A. Awazu, H. Nishimori and S. Nakata, *Collective motion of symmetric camphor papers in an annular water channel*, Phys. Rev. E, 88, 012911 (2013).

[41] K. Nishi, T. Ueda, M. Yoshii, Y. S. Ikura, H. Nishimori, S. Nakata and M. Nagayama, *Bifurcation phenomena of two self-propelled camphor disks on an annular field depending on system length*, Phys. Rev. E 92, 022910 (2015).

[42] K.T. Alligood, T.D. Sauer, J.A. Yorke, *Chaos: An Introduction to Dynamical Systems*, Springer (1996).

[43] V.S. Anishchenko, V. Astakhov, A. Neiman, T. Vadivasova and L. Schimansky-Geier, *Nonlinear dynamics of chaotic and stochastic systems. Tutorial and Modern Developments*, Springer (2007).

[44] M. Balcerzak, D. Pikunov and A. Dabrowski, *The fastest, simplified method of Lyapunov exponents spectrum estimation for continuous-time dynamical systems*, Nonlinear Dyn. 94, 3053-3065 (2018).

[45] S. Newhouse, D. Ruelle and F. Takens *Occurrence of strange Axiom A attractors near quasiperiodic flows on* $T^m, m \geq 3$, Communications in Mathematical Physics, 64(1), 35-40, (1978)

[46] E. Hairer and G. Wanner, *ROS4*, `http://www.unige.ch/~hairer/prog/stiff/Oldies/ros4.f`, accessed: 2021-08-28 (1992).

[47] E. Hairer, *Fortran Codes*, `http://www.unige.ch/~hairer/software.html`, accessed: 2021-08-28.

[48] E. Hairer, S. P. Nørsett and G. Wanner, *Solving Ordinary Differential Equations II: Stiff and Differential-Algebraic Problems, 2nd Edition*, Springer (1996).

[49] E. Hairer and G. Wanner, *Solving Ordinary Differential Equations II: Stiff and Differential-Algebraic Problems, 2nd Edition*, Springer (1996).

[50] H.B. Keller, *Lectures on numerical methods in bifurcation problems*, Applied Mathematics, 217, 50 (1987).

[51] G. Guennebaud, B. Jacob and others, *Eigen*, `http://eigen.tuxfamily.org`, accessed: 2021-08-28 (2010).

[52] B.T. Smith, J.M. Boyle, J.J. Dongarra, B.S. Garbow, Y. Ikebe, V.C. Klema and C.B. Moler, *Matrix Eigensystem Routines, EISPACK Guide*, Lecture Notes in Computer Science , Volume 6, Springer Verlag (1976).

[53] R.B. Lehoucq, D.C. Sorensen and C. Yang, *ARPACK Users Guide: Solution of Large-Scale Eigenvalue Problems with Implicitly Restarted Arnoldi Methods*, SIAM (1998).

[54] H. B. Keller, *Numerical Methods for Two-Point Boundary Value Problems*, Blaisdell, Waltham (1968).

[55] L. B. Rall, *Automatic Differentiation: Techniques and Applications*, Springer (1981).

Part II
Catch and Release Chemotaxis

Catch and Release Chemotaxis

1 Introduction

Chemotaxis in living organisms is essential for maintaining life in terms of acquiring nutrition or avoiding hazards [2–6]. In general, due to chemotaxis, living organisms will move to another place after consuming the nutrition at their original location. Although many types of artificial self-propelled objects have demonstrated chemotaxis, most self-propelled motions are one-directional along the concentration gradient of the chemical stimulus; [7–17] this is because most objects cannot usually move both towards and away from a region possessing the highest concentration of the chemical stimulus. For example, 2-hexyldecanoic-acid-containing droplets induced by the Marangoni flow, whose driving force is the difference of surface tension, exhibited positive chemotaxis towards HCl stimulus. [7, 11] As another example, a 1-decanol droplet exhibited the reversal of its chemotactic direction with the addition of an aqueous NaCl solution. [10] Both examples are one-directional; they never return from the region of high concentration. In this paper, unlike these, we propose a new type of self-propelled system that consists of a 6-methyl coumarin (6-MC) disk and Na_3PO_4 tablet, where the 6-MC disk is able to repeatedly move both ways; towards and away from the Na_3PO_4 tablet. The experimental system is described in Fig.1. The mechanisms of this process are discussed in terms of the surface tension, chemical reaction between 6-MC and OH^-, and spatial gradient of the base. The experimental results are qualitatively reproduced by numerical calculations based on the reaction-diffusion system coupled with the equation of motion.

2 Experimental Results

Experiments were conducted with different amounts and distributions of solid Na_3PO_4. For each setup, we calculated the time-dependent variation of the distance from the center L, and the speed v (Fig.2). In the cases that the amounts of Na_3PO_4 tablet added were zero and small(mass:20 mg, diameter:3 mm, thickness:4 mm), no evidence of chemotaxis was observed (Fig.2(a) and (b), resp.). When a moderately sized Na_3PO_4 tablet(mass:0.5 g, diameter:10 mm, thickness:4 mm) was added, repeated catch-and-release chemotaxis was observed(Fig.2(c)). When $L > 10$ mm, the movement speed of the disk was essentially constant around 10 mm/s, which means that it moved

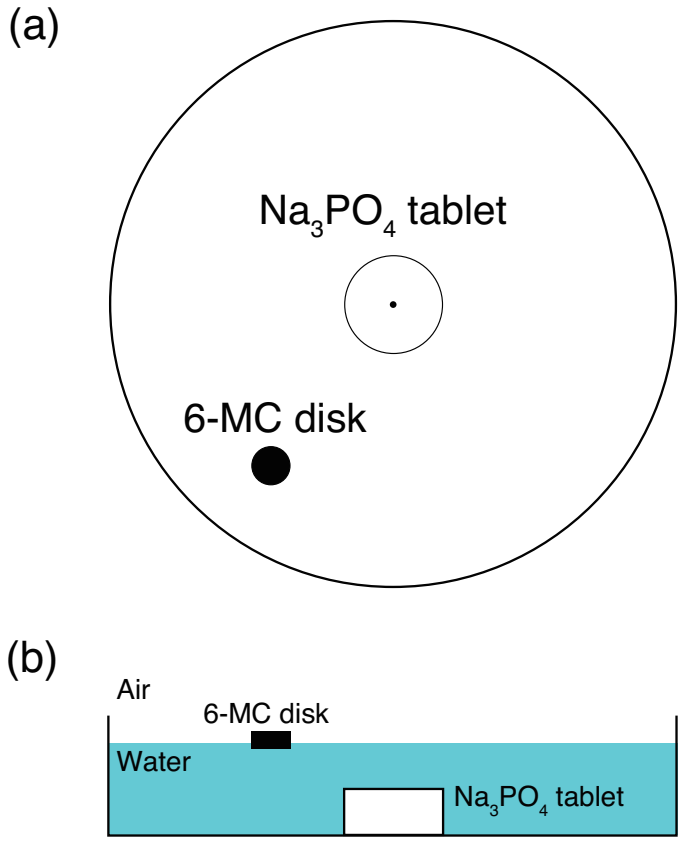

Figure 1: Explanation of the experimental setup. (a) Top view. (b) Side view.

continuously. When a large amount of Na_3PO_4 powder introduced and distributed (distribution diameter:~65 mm, mass:3.0 g), oscillatory motion between the resting and motion states occurred in an unspecified place (Fig.2(d-1)). The characteristic time-dependent motion of Figure 2(c) is depicted in Figure 3. It clearly shows that the disk was caught by the Na_3PO_4 tablet and released after a while.

The surface tension of the water phase was measured to investigate the driving force of the motion of the 6-MC disk with or without the reaction between 6-MC and OH^- that was obtained by the dissolution of Na_3PO_4 (Fig.4). The saturation concentration of 6-MC in water was determined to be ~5 mM. The surface tension of water decreased with increasing 6-MC concentration (Fig.4(a)). On the other hand, for an aqueous solution of 5 mM 6-MC, the surface tension of the system increased up to the surface tension of pure water with increasing Na_3PO_4 concentration (Fig.4(b)). Note that the surface tension of the water phase was independent of the concentration of Na_3PO_4 (filled circles in Fig.4(b)).

The pH near the water surface was evaluated spatiotemporally using bromothymol blue (BTB) as an indicator to investigate the effect of the Na_3PO_4 concentration on the characteristic features of the disk motion. Here, $t = 0$ corresponds to the time at which the Na_3PO_4 tablet was placed in the water phase at the bottom of the chamber. The pH values were obtained based on the calibration curve on the grayscale and measured pH. Figure 5 shows the time-dependent evolution of the pH near the water surface, analyzed from the side view of a rectangular chamber (See Appendix A for detailed information), with the addition of different sized Na_3PO_4 tablets or the distribution of Na_3PO_4 powder. No 6-MC disk was floated on the aqueous phase in this experiment. The pH increased at the bottom of the water phase in both the vertical and horizontal from the Na_3PO_4 tablet. When a smaller Na_3PO_4 tablet was used, the pH near the water surface was lower than 7.3 (Fig. 5(a)). With a moderately sized Na_3PO_4 tablet, the pH at the center of the water surface reached 7.3 and the difference in the pH was greater than 0.5 at $5 \leq t \leq 7$ min (Fig. 5(b)). When a larger amount of Na_3PO_4 was used, the pH near the water surface was higher than 8 and the spatial gradient of the pH was minimal (Fig. 5(c)).

3 Discussion

Based on the experimental results and related preceding studies [18–21], we discuss the dependence of the mechanism of characteristic motion on the size of the Na_3PO_4 tablet. The driving force for the motion of the 6-MC disk is derived from the distribution of 6-MC on the water since hydrophobic 6-MC molecules absorbed on the water surface can decrease the surface tension of the water phase (Fig. 4(a)). Conversely, the increase in the surface tension of

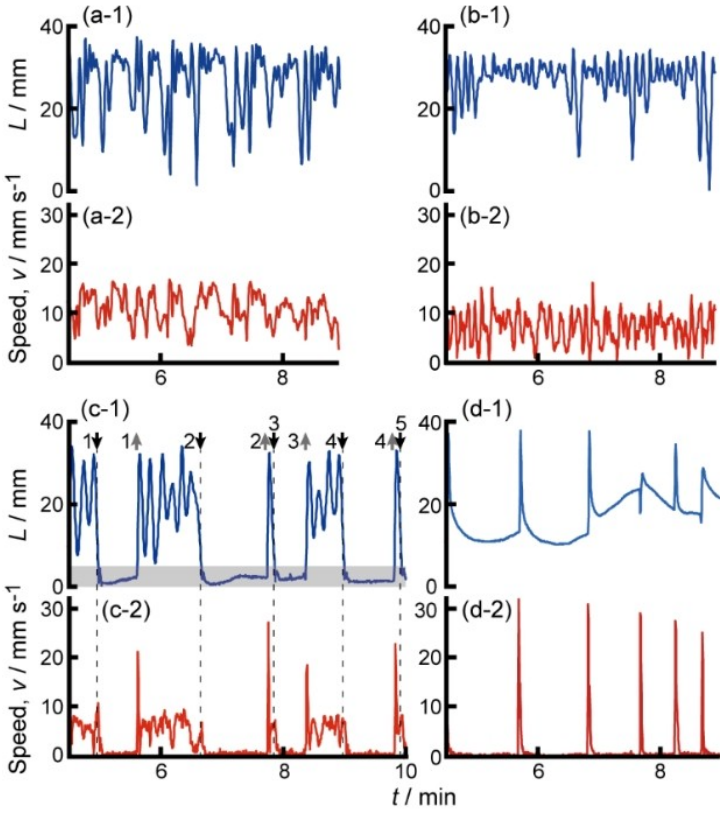

Figure 2: Time-dependent variations of the distance from the center (a-1, b-1, c-1 and d-1), and the velocity (a-2, b-2, c-2 and d-2). Each has a different sized Na_3PO_4 tablet ((a) mass: 0.0 g,(b) mass:20 mg, diameter:3 mm, thickness:4 mm,(c) mass:0.5 g, diameter:10 mm, thickness:4 mm) or Na_3PO_4 powder ((d)mass:3.0 g, distribution diameter of solid Na_3PO_4:~65 mm) in water phase. In (c-1), the gray zone denotes the range of L ($0 \leq L \leq 5$mm) corresponding to the radius of the Na_3PO_4 tablet. The downward and upward arrows in (c-1) denote the times when the state changes from a continuous state to a catch state and vice versa, respectively. (Cropped Figure 1 from the published version [1])

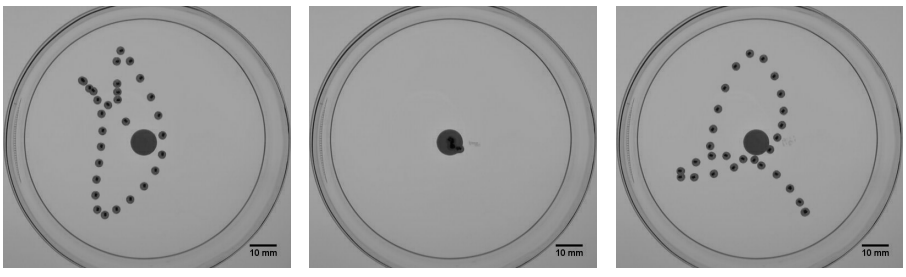

(a) (b) (c)

Figure 3: Composited images of the time-lapse view of the disk motion that corresponds to Figure 2(c). The interval between frames is 1.0 s. (a) First 30 seconds. (b) 39 seconds following (a). (c) 30 seconds following (b).

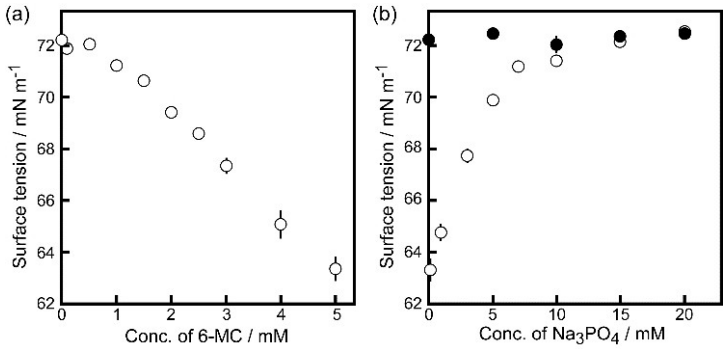

Figure 4: The surface tension of the water phase with different dissolved concentrations of (a) 6-MC and (b) Na_3PO_4. (b) The surface tension of the water surface with (empty circles) and without (filled circles) 5 mM 6-MC. (Cited Figure 3 from the published version [1])

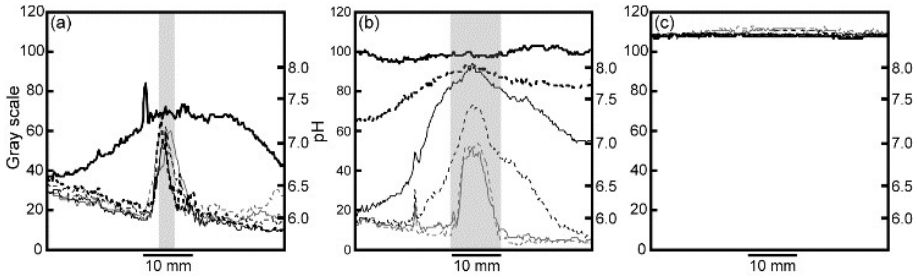

Figure 5: Time-dependent variations of the color of BTB indicator in gray scale (left vertical axis) and corresponding pH (right vertical axis) for the water phase upon the addition of different sized Na_3PO_4 tablets((a) mass:20 mg, diameter:3 mm, (b) mass:0.5 g, diameter:10 mm) and Na_3PO_4 powder ((c)mass:3.0 g, distribution diameter of solid Na_3PO_4:~65 mm) at t =3 min (dotted gray thin line), 4 min (thin gray line), 5 min (dotted thin line), 6 min (thin line), 7 min (dotted thick line) and 9 min(thick line).t = 0 when an Na_3PO_4 tablet or powder was placed into the water phase. The gray zones in (a) and (b) denote the position of the Na_3PO_4 tablet determined from a side view image of the cell. (Cited Figure 4 from the published version [1])

the water phase with 5 mM 6-MC up to that pure water with the addition of Na_3PO_4 (Fig. 4(b)) suggests that the 6-methylcoumaric acid ion (6-MCA$^-$), formed by the reaction of 6-MC with OH^-, is not the driving force of the disk motion. The above result is because hydrophilic 6-MCA$^-$ readily dissolves in the water phase, which makes the surface tension difficult to decrease due to the lower surface concentration of 6-MCA$^-$. That is, the 6-MC disk does not move during the chemical reaction. Here, OH^- is produced from the reaction of water with ${PO_4}^{3-}$, as follows:

$$PO_4^{3-} + H_2O \rightarrow HPO_4^{2-} + OH^-. \quad (1)$$

The continuous motion of the disk under the influence of a small amount of Na_3PO_4 (Fig. 2(a) and (b)) suggests that 6-MC molecules are developed continuously from the disk to the water surface owing to their hydrophobic nature. Figure 5(a) suggests that the hydrolysis of 6-MC, shown in Equation (2), is limited owing to the low pH of the system [21]:

$$\text{6-MC} + OH^- \rightarrow \text{6-MCA}^-. \quad (2)$$

Therefore, continuous motion is observed when a small amount of Na_3PO_4 is used.

The mechanism of the catch-and-release chemotaxis observed when a moderate quantity of Na_3PO_4 is used (Fig. 2(c)) is illustrated schematically in Figure 6. In-State I, when the 6-MC disk approaches the water surface above the Na_3PO_4 tablet, the 6-MC molecules developed in the direction of motion are converted to 6-MCA$^-$ by reaction with OH^-. The 6-MC disk moves in the direction of the region with higher surface tension since the surface tension of the aqueous solution of 6-MCA$^-$ is similar to that of pure water. That is, the 6-MC disk further approaches the air-water interface above the Na_3PO_4 tablet. Figure 2(c) suggests that the 6-MC disk is caught by the Na_3PO_4 tablet owing to the higher concentration of OH^- above the tablet. The disk speed decreases to zero at L <5 mm because the reaction of 6-MC and OH^- predominantly occurs in the vicinity of the interface above the tablet. Then, the disk stops at the location with the highest surface tension, i.e., the midpoint of the location of the Na_3PO_4 tablet and such a Catch state is maintained during the reaction (State II) at $0 \leq L < 5$mm. When the concentration of OH^-around the disk decreases to a threshold value owing to the consumption of $OH^-$by its reaction with 6-MC and the diffusion limit of OH^-formed from the reaction of water with ${PO_4}^{3-}$, the disk accelerates across the water surface in a Release motion (State III). The results in Figure 5(b) justify the argument that the spatial pH gradient in the range of $5 \leq L < 10$mm induces the Catch-and-Release chemotaxis. Clear observation of the positive chemotaxis upon the addition of Na_3PO_4 powder suggests that the dissolution rate of Na_3PO_4 from the powder is higher than that from the compressed Na_3PO_4 tablet.

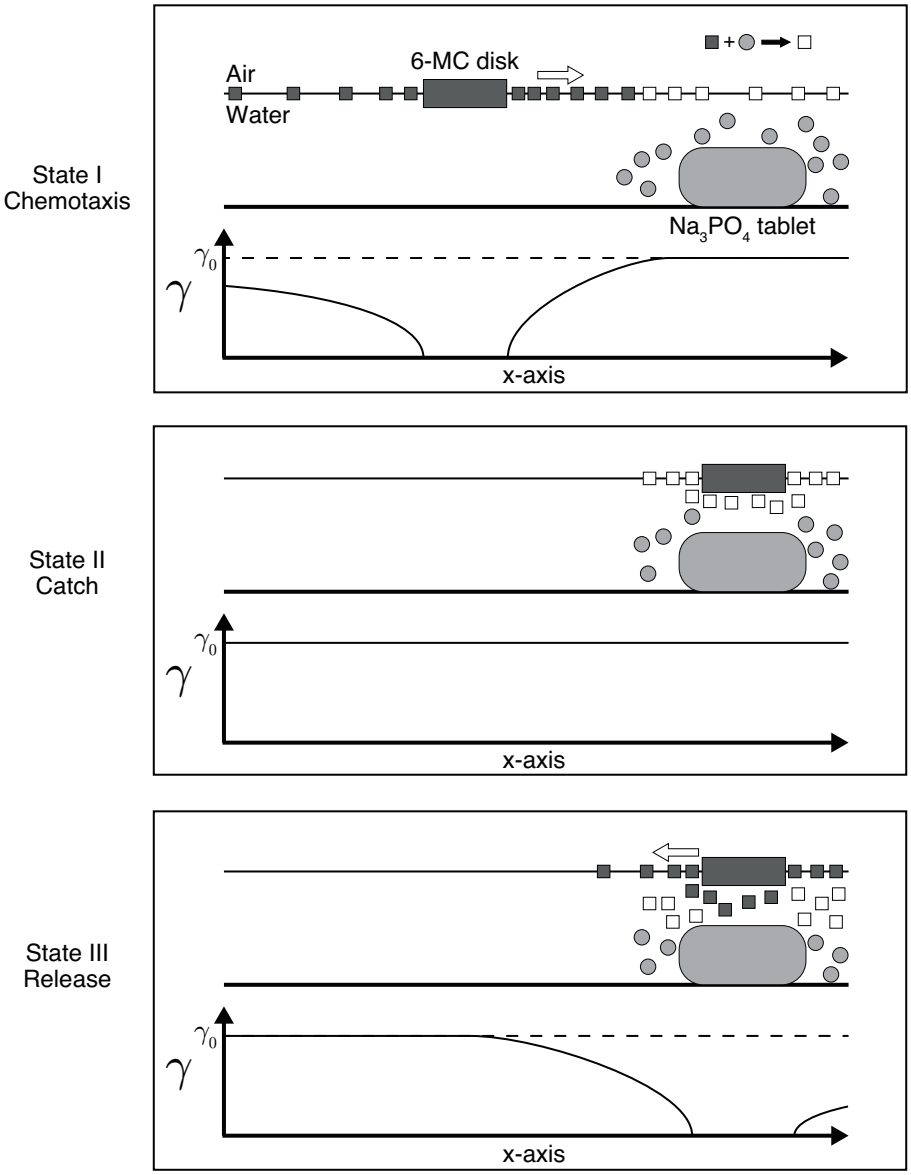

Figure 6: Schematic illustration of catch-and-release chemotaxis mechanism consistent with the results presented in Fig. 2(c). (Upper) Side view of the 6-MC disk, Na_3PO_4 tablet, 6-MC molecules (filled squares), 6-MCA$^-$ (empty squares) and OH^- (filled circles) formed by the reaction of ${PO_4}^{3-}$ with water at the air-water interface. (Lower) The surface tension γ along the x-axis for States I, II and III. γ_0 is the surface tension of pure water.

Oscillatory motion was observed irrespective of the location of the chemical stimulus source when a large amount of distributed solid Na_3PO_4 was used (Fig. 2(d)), suggesting that the concentration of OH^- across the entire water phase rapidly reached the threshold value required for oscillatory motion. The small spatial pH gradient at high pH values in Figure 5(c) supports this argument. The mechanism of the oscillation between motion and rest is similar to those noted in previous studies [18, 20, 21]. Figure 6 suggests that different features of the disk motion, i.e., continuous motion, Catch-and-Release chemotaxis, and universal oscillatory motion, are determined by the concentration of OH^- and its spatial gradient at the air-water interface.

To theoretically determine the mechanism of the 6-MC disk motion as a function of the distribution of solid Na_3PO_4, we introduced a mathematical model based on the reaction-diffusion equation and the equation of motion. The assumptions in the model are as follows:

1. A self-propelled object such as a 6-MC disk exhibits one-dimensional motion along the x-axis in a narrow rectangular channel, $(0, L_c) \times (0, \delta y)$, where $\delta y \ll 1$.

2. The size of the base tablet is varied to represent the change in the distribution of solid Na_3PO_4.

3. OH^- is immediately supplied from the base tablet to the water surface owing to the shallowness of the water phase.

4. 6-MCA^- produced by the reaction of 6-MC with OH^- immediately dissolves in the bulk phase.

The mathematical model for $u(x,t), v(x,t)$, and $x_c(t)$ based on assumptions 1-4 is expressed as in Equation (3), where $u(x,t), v(x,t)$, and $x_c(t)$ are the concentration of 6-MC and OH^- near the water surface in the aqueous phase, and the center position of the 6-MC disk, respectively [18, 20, 22].

$$\begin{cases} \dfrac{\partial u}{\partial t} & = d_u u_{xx} - k_1 u - k_2 uv + F(u, x, x_c; r_0), \\ \dfrac{\partial v}{\partial t} & = d_v v_{xx} - k_2 uv + G(v, x, x_p; r_1), \\ m\dfrac{d^2 x_c}{dt^2} & = \delta y(\gamma(u(x_c + r_0, t)) - \gamma(u(x_c - r_0, t))) - \mu \dfrac{dx_c}{dt}, \end{cases} \tag{3}$$

where d_u and d_v are the diffusion coefficients of 6-MC and OH^-, respectively. k_1 and k_2 are the rate constants for the dissolution of 6-MC in the water phase and the reaction of 6-MC and OH^-, respectively. m, μ, r_0, and r_1 are the mass of the 6-MC disk, the friction coefficient of the 6-MC disk motion, and the radii of the 6-MC and base disks, respectively. x_p denotes

the center position of the base disk. Functions F and G, which correspond to the supplementation of 6-MC and OH^-, are given by Equation (4) and (5), respectively:

$$F(u,x,x_c;r_0)=\begin{cases} s_u\left(1-\dfrac{u}{u_0}\right), & \text{if } |x-x_c|\le r_0,\\ 0, & \text{otherwise,}\end{cases} \tag{4}$$

$$G(v,x,x_p;r_1)=\begin{cases} s_v\left(1-\dfrac{v}{v_0}\right), & \text{if } |x-x_p|\le r_1,\\ 0, & \text{otherwise,}\end{cases} \tag{5}$$

where s_u and s_v are the rate coefficients for 6-MC molecules supplied from the disk and OH^- supplied from the base disk, respectively. u_0 and v_0 are the saturation concentrations of 6-MC and OH^- on the water surface, respectively.

The surface tension γ depending on u is described by the monotonically decreasing function, as shown in Equation (6):

$$\gamma(u)=\frac{\gamma_1}{1+\left(\dfrac{u}{u_1}\right)^n}+\gamma_0, \tag{6}$$

where γ_0 is the surface tension at the critical micelle concentration and $\gamma_0+\gamma_1$ is the surface tension of pure water. u_1 and n are a positive real number and a positive integer, respectively.

We also introduce the following dimensionless variables and parameters to normalize Equations (3)-(6):

$$\tau=k_1t, y=\frac{x}{r_0}, \bar{u}=\frac{u}{u_0}, \bar{v}=\frac{v}{v_0}, y_c(\tau)=\frac{x_c(t)}{r_0},$$
$$D_u=\frac{d_u}{r_0^2k_1}, D_v=\frac{d_v}{r_0^2k_1},$$
$$K_2=\frac{v_0k_2}{k_1}, K_3=\frac{u_0k_2}{k_1}, S_u=\frac{s_u}{u_0k_1}, S_v=\frac{s_v}{v_0k_1},$$
$$y_p=\frac{x_p}{x_0}, R_1=\frac{r_0}{r_1}, \mu_1=\frac{\mu}{mk_1}, \Gamma_0=\frac{\delta y\gamma_0}{m\gamma_0k_1^2}, \Gamma_1=\frac{\delta y\gamma_1}{m\gamma_0k_1^2}, \alpha=\frac{u_0}{u_1}.$$

Upon substituting the expressions for $\tau, y, \bar{u}, \bar{v}, y_c$, and y_p in the original notation, the dimensionless mathematical model described by Equations (7)-(10) is derived from Equations (3)-(6).

$$\begin{cases} \dfrac{\partial u}{\partial t} &= D_uu_{xx}-u-K_2uv+F(u,x,x_c),\\ \dfrac{\partial v}{\partial t} &= D_vv_{xx}-K_3uv+G(v,x,x_p;R_1),\\ \dfrac{d^2x_c}{dt^2} &= \Gamma(u(x_c+1,t))-\Gamma(u(x_c-1,t))-\mu_1\dfrac{dx_c}{dt},\end{cases} \tag{7}$$

$$F(u,x,x_c)=\begin{cases}S_u\,(1-u)\,, & \text{if } |x-x_c|\le 1,\\ 0, & \text{otherwise,}\end{cases} \tag{8}$$

$$G(v,x,x_p;R_1)=\begin{cases}S_v\,(1-v)\,, & \text{if } |x-x_p|\le R_1,\\ 0, & \text{otherwise,}\end{cases} \tag{9}$$

$$\Gamma(u)=\frac{\Gamma_1}{1+(\alpha u)^n}+\Gamma_0, \tag{10}$$

The notations of the variables and coefficients $y, \tau, \bar{u}, \bar{v}, y_c$ and y_p are replaced with the original ones x, t, u, v, x_c and x_p (resp.) for simplicity.

We apply the following initial and boundary conditions for Equation (7):

$$u(x,0)\equiv 0, v(x,0)\equiv v_0(x), x_c(0)=x_0, \frac{dx_c}{dt}(0)=x_1, \tag{11}$$

and

$$u(0,t)=u(L_c,t), \frac{\partial u}{\partial x}(0,t)=\frac{\partial u}{\partial x}(L_c,t), \tag{12}$$

$$v(0,t)=v(L_c,t), \frac{\partial v}{\partial x}(0,t)=\frac{\partial v}{\partial x}(L_c,t). \tag{13}$$

As the base disk is initially located at the bottom of the water phase, we define the initial function $v_0(x)$ as follows:

$$v_0(x)=\begin{cases}1, & \text{if } |x-x_p|\le R_1,\\ 0, & \text{otherwise.}\end{cases} \tag{14}$$

We introduce a periodic boundary condition to eliminate the change in the disk motion due to the boundary effect. As the initial condition is perturbed, the 6-MC disk moves in a positive direction. When R_1 is small, the 6-MC disk moves at a uniform velocity without responding to the base disk (Fig. 7(a)). The deceleration and subsequent acceleration observed in Figure 7(a) are obtained when the 6-MC disk passes through the chemical stimulus since the disk is sensitive to the stimulus. When R_1 is large, the 6-MC disk stops on the water surface above the base disk and then moves to escape from the base disk (Fig. 7(b)). When R_1 is approximately equal to L_c, the 6-MC disk exhibits oscillatory motion (Fig. 7(c)). This oscillatory motion is similar to the phenomenon observed in a camphoric acid-phosphate system [20]. Thus, three features of the disk motion in Figure 7(a), (b) and (c), which are similar to the experimental results in Figure 2(b), (c) and (d), respectively, were qualitatively reproduced by the mathematical model.

4 Conclusion

Catch-and-Release chemotaxis can be repeatedly induced using an inanimate self-propelled object. Chemotaxis and Catch motion is induced by the

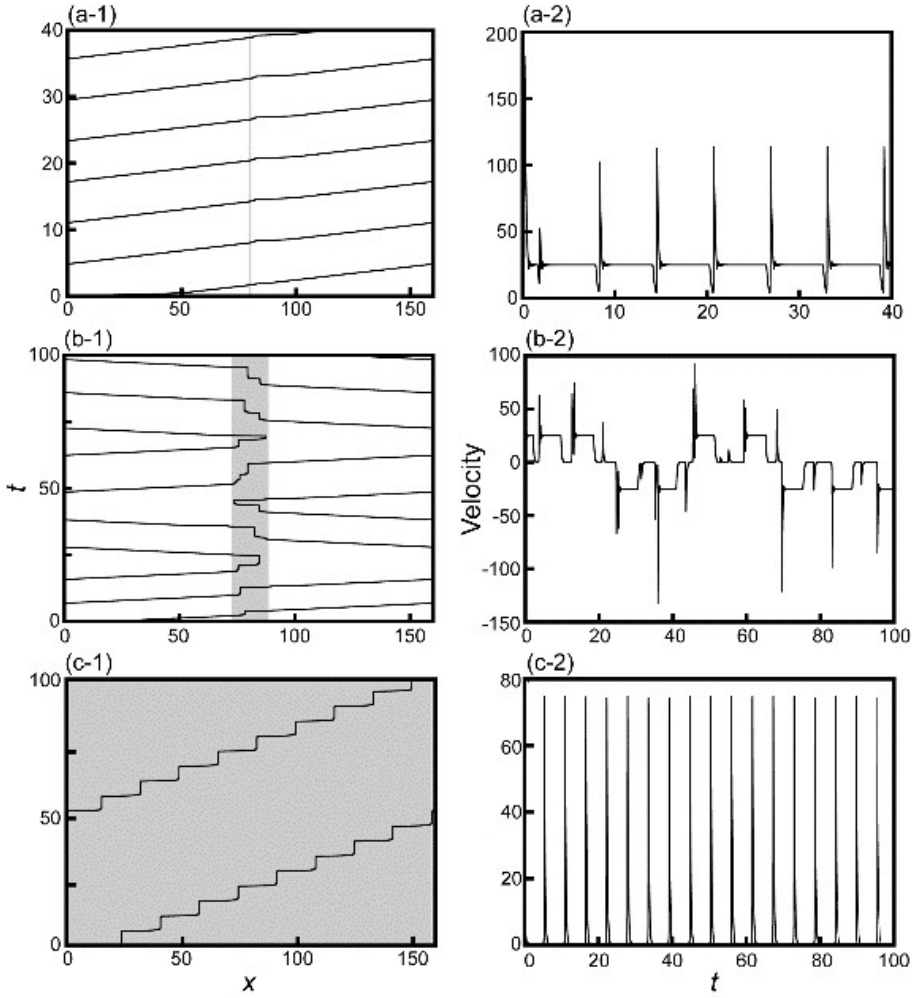

Figure 7: Numerical results: (1) Time-space diagram and (2) temporal change in the velocity of the disk motion based on Eqs. (7)-(10) at R_1=(a) 0.3, (b) 8.0 and (c) 60.0. $D_u = 4.0, D_v = 0.2, K_2 = 1600, K_3 = 2000, S_u = 0.55, S_v = 0.125, y_p = 80, \mu_1 = 5.0, \Gamma_0 = 0, \Gamma_1 = 1.7 \times 10^5, \alpha = 10.0, n = 8$ and $L_c = 160$. Gray regions in (1) denote the locations of the base. (Cited Figure 6 from the published version [1])

gradient in the surface tension. That is, the 6-MC disk moves toward the region of highest surface tension due to the increase in pH near the Na_3PO_4 tablet; this is because 6-MC molecules decrease the surface tension. During the hydrolysis reaction between 6-MC and OH^-, the 6-MC disk is caught on the water surface above the Na_3PO_4 tablet because the 6-MC disk lacks the driving force for motion. When the reaction goes to completion owing to the exhaustion of OH^- near the water surface, the 6-MC disk escapes from its location on the water surface above the Na_3PO_4 tablet; that is, the Release motion is triggered. Thus, the Catch-and-Release chemotaxis continues while the pH gradient around the Na_3PO_4 tablet is maintained. Although similar behaviors to the experimental results can be reproduced qualitatively by numerical calculations, one-dimensional calculations predict that the 6-MC disk approaches the base regardless of whether positive chemotaxis occurs. Future work will focus on developing of a two-dimensional mathematical model to overcome this problem.

A Miscellaneous Experimental Setup

A rectangular plastic vessel (95 mm×95 mm×27 mm) filled with distilled water (54 mL; water depth: 6 mm) was used for measuring pH in Chapter 2.

References

[1] Y. Yasugahira, Y. Tatsumi, O. Yamanaka, H. Nishimori, M. Nagayama, S. Nakata, *Catch and Release Chemotaxis*, ChemSystemsChem e2100031 (2021).

[2] J. Adler, *Chemotaxis in Bacteria*, Science, 153, 3737, 708-716 (1966).

[3] C. A. Parent, P. N. Devreotes, *A Cell's Sense of Direction*, Science, 284, 5415, 765-770 (1999).

[4] A. V. Vorotnikov, *Chemotaxis: Movement, direction, control*, 76, 1528–1555 (2011).

[5] G. L. Hazelbauer, *Bacterial Chemotaxis: The Early Years of Molecular Studies*, Annual Review of Microbiology, 66, 285-303 (2012).

[6] S. Bi, V. Sourjik, *Stimulus sensing and signal processing in bacterial chemotaxis*, Current Opinion in Microbiology, 45, 22-29 (2019).

[7] I. Lagzi, S. Soh, P. J. Wesson, K. P. Browne, B. A. Grzybowski, *Maze Solving by Chemotactic Droplets*, Journal of the American Chemical Society, 132, 1198–1199 (2010).

[8] J. Palacci, C. Cottin-Bizonne, C. Ybert, L. Bocquet, *Osmotic traps for colloids and macromolecules based on logarithmic sensing in salt taxis*, Soft Matter, 8, 980–994 (2012).

[9] K. K. Dey, S. Bhandari, D. Bandyopadhyay, S. Basu, A. Chattopadhyay, *The pH Taxis of an Intelligent Catalytic Microbot*, Small, 9, 1916–1920 (2013).

[10] J. Čejková, M. Novák, F. Štěpánek, M. M. Hanczyc, *Dynamics of Chemotactic Droplets in Salt Concentration Gradients*, Langmuir, 30, 11937–11944 (2014).

[11] P. Lovass, M. Branicki, R. Tóth, A. Braun, K. Suzuno, D. Ueyama, I. Lagzi, *Maze solving using temperature-induced Marangoni flow*, RSC Advances, 5, 48563–48568 (2015).

[12] C. Jin, C. Krüger, C. C. Maas, *Chemotaxis and autochemotaxis of self-propelling droplet swimmers*, PNAS, 114, 5089–5094 (2017).

[13] A. Joseph, C. Contini, D. Cecchin, S. Nyberg, L. Ruiz-Perez, J. Gaitzsch, G. Fullstone, X. Tian, J. Azizi, J. Preston, G. Volpe, G. Battaglia, *Chemotactic synthetic vesicles: Design and applications in blood-brain barrier crossing*, Science Advances, 3, e1700362 (2017).

[14] B. Liebchen, H. Löwen, *Synthetic Chemotaxis and Collective Behavior in Active Matter*, Accounts of Chemical Research, 51 (12), 2982-2990 (2018).

[15] S. Holler, C. Porcelli, I. A. Ieropoulos, M. M. Hanczyc, *Transport of Live Cells Under Sterile Conditions Using a Chemotactic Droplet*, Scientific Reports, 8, 8408(2018).

[16] Y. Ji, X. Lin, Z. Wu, Y. Wu, W. Gao, Q. He, *Macroscale Chemotaxis from a Swarm of Bacteria-Mimicking Nanoswimmers*, Angewandte Chemie International Edition, 58, 12200–12205 (2019), Angewandte Chemie, 131, 12328–12333 (2019).

[17] L. Baraban, S. M. Harazim, S. Sanchez, O. G. Schmidt, *Chemotactic Behavior of Catalytic Motors in Microfluidic Channels*, Angewandte Chemie International Edition, 52, 5552-5556 (2013), Angewandte Chemie, 125, 5662–5666 (2013).

[18] S. Nakata, M. Nagayama, H. Kitahata, N. J. Suematsu, T. Hasegawa, *Physicochemical design and analysis of self-propelled objects that are characteristically sensitive to environments*, Physical Chemistry Chemical Physics, 17, 10326–10338 (2015).

[19] N. J. Suematsu, S. Nakata, *Evolution of Self-Propelled Objects: From the Viewpoint of Nonlinear Science*, Chemistry - A European Journal, 24, 6308 (2018).

[20] *Self-Organized Motion: Physicochemical Design Based on Nonlinear Dynamics* (Edited by S. Nakata, V. Pimienta, I. Lagzi, H. Kitahata, N. J. Suematsu), The Royal Society of Chemistry, Cambridge (2019).

[21] S. Nakata, Y. Irie, N. J. Suematsu, *Self-Propelled Motion of a Coumarin Disk Characteristically Changed in Couple with Hydrolysis on an Aqueous Phase*, The Journal of Physical Chemistry B, 123, 4311-4317 (2019).

[22] Y. Satoh, Y. Sogabe, K. Kayahara, S. Tanaka, M. Nagayama, S. Nakata, *Self-inverted reciprocation of an oil droplet on a surfactant solution*, Soft Matter, 13, 3422-3430 (2017).

Acknowledgements

I would like to thank Prof. Nagayama for useful discussions and his very generous support. I wish to thank Dr. Okamoto for advice on my numerical calculations. For the second part, I am grateful to Prof. Nakata for insightful discussions. I also want to thank the people who contributed to conducting the experiments.

In addition, I would like to thank all the secretaries in the laboratory. They kindly supported me during my school years. Finally, I would like to express my sincere gratitude to the members and ex-members of the laboratory and all the people I got familiar with in the university for being nice and friendly with me. They really helped me to keep myself in good condition.